

# Performance Improvement of Deception Jamming Against SAR Based on Minimum Condition Number

Bo Zhao, *Member, IEEE*, Lei Huang, *Senior Member, IEEE*, Feng Zhou, *Member, IEEE*, and Jihong Zhang

**Abstract**—This paper proposes a new approach to improve the error performance of the synergy netting deception jamming against synthetic aperture radar (SAR). The existing methods cannot tackle the issue of error amplification induced by the linear equations constructed for jamming coefficients calculation. To handle this problem, we develop an optimal layout for radar receivers to minimize the effect of the error by minimizing the condition number, which measures the sensitivity of the synergy deception jamming system to the perturbation. It is revealed that the devised approach relies little on the SAR kinematic parameters. To further improve the error performance of the jamming system, collaborative receivers, which provide more observations of time difference of arrivals, are introduced to perform a linear least-squares estimation. The error reduction level due to the cooperative receivers is analyzed. Simulation results are provided to illustrate the superiority of the proposed method.

**Index Terms**—Condition number, deception jamming, optimal layout, synthetic aperture radar (SAR).

## I. INTRODUCTION

THE synthetic aperture radar (SAR) is an effective way for high-accuracy terrain observation. It has been applied to resource remote sensing, geographical mapping, war zone surveillance, precision guidance, etc. [1]–[8]. The electromagnetic countermeasure to SAR has attracted much attention in radar community with the increasing application of SAR [9]–[11]. SAR parameters vary flexibly according to the imaging demand, which results in the game between the SAR and jammer. Being in a passive position, the jammer is blind to the SAR parameters. Therefore, the acquirability and accuracy of the SAR parameters, which determine the effectiveness of SAR jamming, are the important metrics in SAR jamming research.

Manuscript received March 27, 2016; revised June 22, 2016 and August 5, 2016; accepted September 21, 2016. Date of publication October 23, 2016; date of current version February 13, 2017. This work was supported by the Natural Science Foundation of China under Grant U1501253, Grant U1430123, Grant 61201283, Grant 61471284, and Grant 61522114, the Foundation for the Author of National Excellent Doctoral Dissertation of China under Grant 201448, the Natural Science Foundation of Guangdong Province under Grant 2015A030311030, the Foundation of Shenzhen under Grant ZDSYS201507081625213 and Grant KC2015ZDYF0023A, the Young Scientist Award of Shaanxi Province under Grant 2015KJXX-19 and Grant 2016KJXX-82, and the China Postdoctoral Science Foundation under Grant 2015M582413. (*Corresponding author: Lei Huang*)

B. Zhao, L. Huang, and J. Zhang are with the College of Information Engineering, Shenzhen University, Shenzhen 518060, China (e-mail: b\_zhao@126.com; dr.lei.huang@ieee.org; zhangjh@szu.edu.cn).

F. Zhou is with the National Laboratory of Radar Signal Processing, Xidian University, Xi'an 710071, China (e-mail: fzhou@mail.xidian.edu.cn).

Color versions of one or more of the figures in this paper are available online at <http://ieeexplore.ieee.org>.

Digital Object Identifier 10.1109/JSTARS.2016.2614957

Two possible ways are available to guarantee the jamming effect. One is designing the universal jamming method that does not rely on SAR parameters, and the other is improving the performance of the jamming algorithm under error circumstances.

The barrage jamming, which transmits noise-like jamming and works on complex SAR working mode even when its waveform is agile [12], achieves the universality but at the cost of high jamming power [13]–[15]. Deception jamming transmits the modulated coherent jamming and interrupts the SAR with a much lower power than the barrage jamming. It generates verisimilar false target to confuse the radar target recognition [16], [17]. Nevertheless, more detailed SAR kinematic parameters, such as squint angle, grazing angle, and closest range, are required for both false terrain template design and jamming modulation coefficient calculation. The errors introduced by SAR kinematic parameter reconnaissance will accumulate in the jamming modulation and thus reduce the jamming quality. Furthermore, the approximation applied in the deception jamming algorithm also induces errors, which further reduces the imaging quality and the fidelity of the deception jamming scene [18]. This problem has been addressed in the literature. For example, Lin *et al.* analyzed the errors introduced by the approximation of a fast deception jamming method working against side-looking SAR [19]. The deception jamming range was analyzed based on approximation error in [20] and [21]. Zhu *et al.* [22] considered the deception jamming method for squint SAR. Although inaccurate SAR kinematic parameters can also be used to modulate a defocused false scene to cover the real one, the jamming power needs to be increased so that the effectiveness of the coverage can be guaranteed. Moreover, the inaccurate deception jamming can be easily distinguished from the real scene.

To alleviate the dependence of deception jamming on the detailed SAR kinematic parameters, we proposed an algorithm based on multiple receivers in [23]. Multiple receivers are utilized to form a synergy network with the jammer, so that the spatial information provided by multiple receivers can be employed to solve the deception jamming modulation coefficients. By solving a set of linear equations constructed with the measured time difference of arrival (TDOA) in high accuracy [24]–[26], deception jamming coefficients can be obtained without calculating the exact SAR kinematic parameters. This work generalizes the deception jamming scheme to more practical circumstances by taking the measurement error into consideration. To handle the measurement error, the condition number is adopted to analyze the sensitivity of the proposed deception jamming system. The condition number has been widely

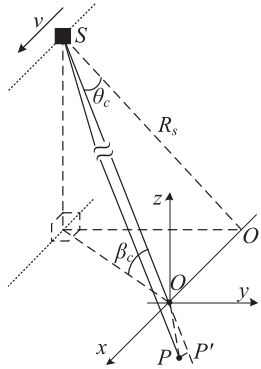


Fig. 1. SAR imaging geometry.

applied to some SAR-related problems to describe the system performance under error perturbation [27]–[29]. But the application of condition number in SAR deception jamming has not yet been addressed in the literature. To fill this gap, this work devises an optimal receiver layout by minimizing the condition number of the deception jamming system. This in turn leads to the minimum sensitivity of the jamming system to the measurement error. Furthermore, collaborative receivers are introduced to further reduce the effect of measurement error on the deception jamming.

The rest of this paper is organized as follows. The geometry model and basic principle of the synergy netting deception jamming algorithm utilizing multiple receivers are illuminated in Section II. Section III devises the optimal layout of multiple cooperative receivers, which is universal to different SAR kinematic parameters and has the least sensitivity to the error perturbation. The effect of the perturbation is further analyzed in Section IV, and the algorithm utilizing collaborative receivers is addressed to improve the effectiveness of synergy netting deception jamming method under error circumstances. Simulation results are given in Section V. Section VI concludes this work.

## II. GEOMETRY MODEL

### A. Geometry Model and Deception Jamming Algorithm

A general SAR imaging geometry model is shown in Fig. 1. The SAR platform, denoted by point  $S$ , operates horizontally along a straight track at a constant speed  $v$ . It works with the squint angle  $\theta_c$  and grazing angle  $\beta_c$  at the beam center. The stop-and-go model [30]–[32] is employed here to simplify the analysis. Set the origin of the coordinates at the intersection of the beam center and the ground at the zero time. The axis  $x$  is parallel to the direction of the velocity of the SAR platform, and axis  $z$  is perpendicular to the ground and positive upwards. Then, the axis  $y$  can be determined by the right-hand rule.  $R_s$  is the distance between the SAR and axis  $x$ , and  $H$  is the altitude of the SAR platform.

To simplify the discussion of deception jamming modulation, the scatterers with different heights are equivalently projected to the  $xOy$  plane. Therefore, an arbitrary scatterer  $P$  with coordinates  $(x_p, y_p, 0)$  is taken as an example to discuss the signal model. The SAR transmits a linear frequency modulation (LFM)

signal, whose parameters do not vary during the deception jamming, given as

$$s(t_r) = \text{rect}(t_r/T_p) \exp(j2\pi f_c t_r) \exp(j\pi\gamma t_r^2) \quad (1)$$

where  $t_r$  is the fast time,  $T_p$  is the pulsedwidth,  $f_c$  is the carrier frequency,  $\gamma$  is the chirp rate,  $j = \sqrt{-1}$ , and  $\text{rect}(\cdot)$  is the rectangular envelope of the LFM signal. Denote the spatial vector from the SAR to scatterer  $P$  by  $\mathbf{r}_P$ , and thus, the single trip instantaneous slant range  $R_p(t_a)$  equals  $\|\mathbf{r}_P\|_2$ , where  $\|\cdot\|_2$  is the Euclidean norm of the vector. Then, the downconverted echo from scatterer  $P$  at slow time  $t_a$  can be described by

$$\begin{aligned} s_p(t_r, t_a) &= \alpha_p \text{rect}\left(\frac{t_r - 2R_p(t_a)/c}{T_p}\right) a_a(t_a) \\ &\times \exp(-j4\pi R_p(t_a)/\lambda) \\ &\times \exp(j\pi\gamma(t_r - 2R_p(t_a)/c)^2) \end{aligned} \quad (2)$$

where  $\alpha_p$  is the scattering coefficient of  $P$ ,  $a_a(t_a)$  is the azimuth envelop function determined by the antenna pattern, and  $c$  is the velocity of light. The instantaneous slant range history describes the characteristic of the scatterer. Therefore, the deception jamming modulation has to be performed scattererwise based on the intercepted SAR signal. Assume that the jammer, which intercepts the SAR signal and transmits the deception jamming, is located at the origin of the coordinate system shown in Fig. 1, and the spatial vector from the SAR to jammer is  $\mathbf{r}_o$ . Denote the instantaneous slant range of the jammer by  $R_o(t_a)$ ; then, the intercepted signal is

$$\begin{aligned} s_o(t_r, t_a) &= \alpha_o \text{rect}\left(\frac{t_r - 2R_o(t_a)/c}{T_p}\right) a_a(t_a) \\ &\times \exp(-j4\pi R_o(t_a)/\lambda) \\ &\times \exp(j\pi\gamma(t_r - 2R_o(t_a)/c)^2). \end{aligned} \quad (3)$$

To generate a false scatterer that appears at the same location as the scatterer  $P$  does, the deception jamming modulation should be

$$\begin{aligned} s_p(t_r, t_a) &= (\alpha_p/\alpha_o)s_o(t_r, t_a) * \delta(t_r - 2R_\Delta(t_a)/c) \\ &\times \exp(-j4\pi R_\Delta(t_a)/\lambda) \end{aligned} \quad (4)$$

where  $*$  is the convolution operator,  $\delta(\cdot)$  is the impulse function,  $\lambda$  is the wavelength,  $\alpha_o$  is the scattering coefficient of  $O$  and thus  $\alpha_p/\alpha_o$  denotes the amplitude modulation, and  $R_\Delta(t_a)$  is the difference between the instantaneous slant ranges of the false scatterer and jammer, namely,  $R_p(t_a) - R_o(t_a)$ .  $\alpha_p$  varies for different false scatterers according to the predesigned template to generate a false scene. As this work is focused on improving the accuracy of delay and phase modulations, the amplitude template is assumed to have been properly designed to fuse with the real scene. Then, the accuracy of  $R_\Delta(t_a)$  directly affects the focusing quality of the deception jamming.

Under the far-field assumption, the signal that the SAR transmits is plane wave, and the beams to different scatterers are parallel to each other. Then, we have  $\mathbf{r}_o \parallel \mathbf{r}_P$ , where  $\parallel$  is the parallel symbol. Using  $\mathbf{r}_\Delta$  and  $\mathbf{r}'_\Delta$  to denote the spatial vector from the jammer to scatterer  $P$  and its projection on  $\mathbf{r}_o$ ,

respectively, the  $R_{\Delta}(t_a)$  is calculated by

$$\begin{aligned} R_{\Delta}(t_a) &= \|\mathbf{r}_p\|_2 - \|\mathbf{r}_o\|_2 \approx \|\mathbf{r}'_{\Delta}\|_2 \\ &= \left\langle \mathbf{r}_{\Delta}, \frac{\mathbf{r}_o}{\|\mathbf{r}_o\|_2} \right\rangle \end{aligned} \quad (5)$$

where  $\langle \cdot, \cdot \rangle$  is the inner product operator. Denote the coordinates of the SAR by  $(vt_a - R_s \tan \theta_c, -R_s \sqrt{\cos^2 \beta_c - \sin^2 \theta_c} / \cos \theta_c, R_s \sin \beta_c / \cos \theta_c)$ . Substituting the coordinates of the SAR and scatterer  $P$  into (5), we obtain

$$\begin{aligned} R_{\Delta}(t_a) &= \frac{-vt_a + R_s \tan \theta_c}{\sqrt{(vt_a - R_s \tan \theta_c)^2 + R_s^2}} x_p \\ &\quad + \frac{R_s \sqrt{\cos^2 \beta_c - \sin^2 \theta_c} / \cos \theta_c}{\sqrt{(vt_a - R_s \tan \theta_c)^2 + R_s^2}} y_p. \end{aligned} \quad (6)$$

Note that the conventional deception jamming algorithm needs to reconnoiter the SAR kinematic parameters item-by-item and then substitute them into (6) to determine  $R_{\Delta}(t_a)$ . The complex electronic reconnaissance for parameters of the non-cooperative SAR introduces measurement errors, which will be accumulated in the calculation of instantaneous slant range difference. This reduces the accuracy of the deception jamming modulation.

For accurate deception jamming modulation, it is the numerical value of  $R_{\Delta}(t_a)$  that matters rather than the exact expression or those SAR kinematic parameters. Notice that (6) not only varies with slow time  $t_a$ , but also is a function of  $x_p$  and  $y_p$ . As a result, (6) can be expressed as

$$R_{\Delta}(t_a) = R_{\Delta}(x_p, y_p) = g_x(t_a)x_p + g_y(t_a)y_p \quad (7)$$

where

$$\begin{aligned} g_x(t_a) &= \frac{-vt_a + R_s \tan \theta_c}{\sqrt{(vt_a - R_s \tan \theta_c)^2 + R_s^2}} \\ g_y(t_a) &= \frac{R_s \sqrt{\cos^2 \beta_c - \sin^2 \theta_c} / \cos \theta_c}{\sqrt{(vt_a - R_s \tan \theta_c)^2 + R_s^2}}. \end{aligned}$$

In each pulse repetition interval (PRI),  $t_a$  can be considered as a constant. Therefore, being independent of the false scatterer's coordinates,  $g_x(t_a)$  and  $g_y(t_a)$  need to be calculated only once during each PRI. Considering  $g_x(t_a)$  and  $g_y(t_a)$  as two unknowns, two additional receivers (or receiving antennas) are necessary to construct a synergy netting deception jamming system with the jammer to determine them. The signals at the jammer and two receivers are in the same form but with different time delays, leading to TDOA. Denoting the receivers by  $A_1(x_1, y_1, 0)$  and  $A_2(x_2, y_2, 0)$ , it follows from (7) that

$$\begin{pmatrix} x_1 & y_1 \\ x_2 & y_2 \end{pmatrix} \begin{pmatrix} g_x(t_a) \\ g_y(t_a) \end{pmatrix} = \begin{pmatrix} R_{\Delta 1}(t_a) \\ R_{\Delta 2}(t_a) \end{pmatrix}. \quad (8)$$

Note that the coordinates of the receivers are the predesigned parameters, which is known as *a priori*. The  $R_{\Delta n}(t_a)$  ( $n = 1, 2$ ) is the TDOA between the  $n$ th receiver and the jammer.

Denoting (8) by  $\mathbf{Ag} = \mathbf{d}$ , the solution matrix can be calculated by

$$\mathbf{g} = \mathbf{A}^{-1} \mathbf{d}. \quad (9)$$

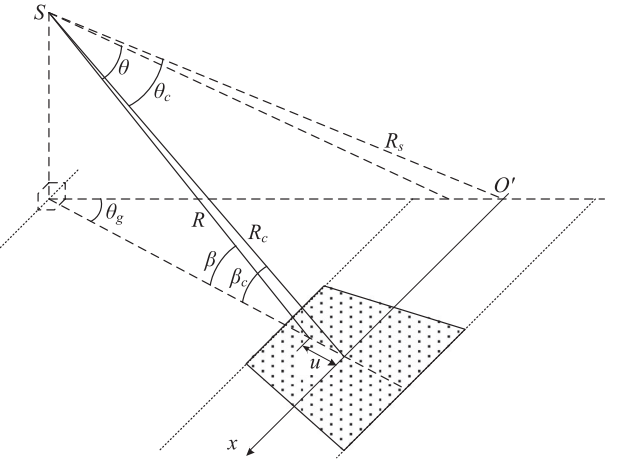


Fig. 2. Far-field approximation error illustration.

The instantaneous slant range difference of the false scatterer  $F$  can be calculated by substituting its coordinates  $(x_F, y_F, 0)$  and the solved coefficients into (7), leading to  $R_{\Delta F}(t_a) = g_x(t_a)x_F + g_y(t_a)y_F$ . Then, the deception jamming of false scatterer  $F$  can be obtained by substituting  $R_{\Delta F}(t_a)$  into (4).

### B. Jamming Area Limitation

To balance the accuracy and computational efficiency, the approximation is usually employed for deception jamming algorithm designing. In the conventional deception jamming scheme, the ignorance of the second- and higher-order terms about  $t_a$  leads to distortion and defocusing of the false scene, especially in the squint SAR imaging mode. Meanwhile, the same reconnoitered parameters are used for different scatterers' modulation, which makes the spatial varying characteristics of the scatterers, such as range migration difference and Doppler chirp rate variation, cannot be included. This leads to a small jamming area limited by the focus depth [21]. Unlike the conventional algorithm, the instantaneous slant range for netting deception jamming scheme is calculated according to (7), which is expressed as a function of the scatterer's coordinates. This allows the jamming modulation parameter to vary with the location of the false scatterer, thereby providing a larger jamming area than the conventional deception jamming scheme. To analyze the limited jamming area by using far-field assumption, the illuminated area of SAR beam is shown in Fig. 2.

In Fig. 2, the illuminated area is shaded with dots,  $R$  is the distance between the SAR platform and an arbitrary scatterer on the projection of the line of sight on the ground,  $R_c$  is the value of  $R$  at the imaging area center,  $u$  is the distance of the arbitrary scatterer from the center,  $\theta$  is the squint angle, and  $\beta$  is the grazing angle. The accurate expressions of  $R$  is

$$R = \sqrt{R_c^2 + u^2 - 2u \cos \beta_c}. \quad (10)$$

Expanding (10) around  $u$  by Taylor series, we have

$$R = R_c - u \cos \beta_c + u^2 \frac{\sin^2 \beta_c}{2R_c} + u^3 \frac{\cos \beta_c \sin^2 \beta_c}{2R_c^2} + \dots \quad (11)$$

For the netting deception jamming scheme, the approximated  $R'$ , instead of  $R$ , is calculated utilizing (6) under the far-field assumption. That is

$$R' = R_c - u \cos \beta_c. \quad (12)$$

In (12), the terms about  $u$  with the second- or higher-order are ignored on the condition that  $R_c \gg u$ . Being a function about  $u$ ,  $R'$  varies with different false scatterer locations. Therefore, the spatial varying characteristic of the scatterers can still be generally described by the slant range calculated by the netting deception jamming algorithm and, thus, a larger jamming area than the conventional deception jamming. The second-order term about  $u$  is considered as the approximation error for further analysis

$$\varepsilon = u^2 \frac{\sin^2 \beta_c}{2R_c}. \quad (13)$$

*1) Range Distortion Limitation:* The error of the slant range in the beam center determines the range location of the false scatterer. When the error  $\varepsilon$  is less than half a range resolution cell  $\rho_r$ , the range distortion it caused is considered not noticeable. Then, we have

$$|u| < \frac{\sqrt{R_c} \rho_r}{\sin \beta_c}. \quad (14)$$

*2) Azimuth Distortion Limitation:* The slant range uncertainty also incurs error in the squint angle, which is related to the Doppler frequency center and determines the azimuth location of the false scatterer. The sine expression for  $\theta$  is

$$\sin \theta = \sin \beta \sin \theta_g = \frac{R_c \cos \beta_c - u}{R' + \varepsilon} \sin \theta_g \quad (15)$$

where  $\theta_g$  is the projection of  $\theta$  on the ground. By utilizing the far-field assumption, the error of  $\sin \theta$  is

$$\begin{aligned} \sin \theta_\Delta &= (R_c \cos \beta_c - u) \sin \theta_g \left( \frac{1}{R'} - \frac{1}{R' + \varepsilon} \right) \\ &= \frac{\cos \beta \sin \theta_g}{R'} \varepsilon < \frac{\varepsilon}{R'}. \end{aligned} \quad (16)$$

Because  $\beta$  and  $\theta_g$  may vary with different SARs, the upper bound of  $\sin \theta_\Delta$  is used for a universal derivation. Assuming the azimuth distortion caused by (16) is smaller than half an azimuth resolution cell  $\rho_a$ , we obtain

$$R \sin \theta_\Delta < \frac{R}{R'} \varepsilon < \frac{\rho_a}{2}. \quad (17)$$

By applying the approximation  $R'/R \approx 1$  and employing the expression of  $\varepsilon$  given in (13), the limitation of azimuth distortion on  $u$  is

$$|u| < \frac{\sqrt{R_c} \rho_a}{\sin \beta_c}. \quad (18)$$

*3) Focusing Quality Limitation:* The scatterers distributing in different distances have different slant range migrations, which also determines the Doppler frequency variation. The Doppler frequency, being at the level of wave length, is more sensitive to the approximation error than the range migration, which is at the level of resolution cell. Therefore, the analysis of

Doppler frequency error is able to reveal the effect of far-field assumption error on deception jamming focusing quality. The Doppler bandwidth is

$$B_a = \frac{2\Theta_a v \cos \theta_c}{\lambda} \quad (19)$$

where  $\Theta_a$  is the beamwidth. Note that, in a SAR system, the speed  $v$  and wavelength  $\lambda$  are usually constants. This means that the Doppler bandwidth for different scatterers is the same. However, due to the skewing imaging beam, its intersected area on the ground is not a rectangular but a trapezoid. So the lengths of synthetic aperture for the scatterers with different distances to the SAR platform are different, which lead to different synthetic aperture times. The synthetic aperture time  $T_a$  can also be calculated utilizing  $\Theta_a$ , which is given as

$$T_a = \frac{R\Theta_a}{v \cos \theta_c}. \quad (20)$$

The error of Doppler chirp rate can be calculated utilizing (13) as

$$\Delta K = B_a \left( \frac{v \cos \theta_c}{R\Theta_a} - \frac{v \cos \theta_c}{(R + \varepsilon)\Theta_a} \right). \quad (21)$$

The Doppler chirp rate determines the change rate of Doppler frequency. Therefore, the phase error accumulates with the slow time  $t_a$  increasing and achieves the maximum value at the ends of the synthetic aperture, say,  $t_a = \pm T_a/2$ . Then, we have

$$\Delta f_D = \Delta K \frac{T_a^2}{4} = \frac{\varepsilon \Theta_a R}{4\rho_a (R + \varepsilon)} \approx \frac{\lambda}{8\rho_a^2} \varepsilon. \quad (22)$$

The approximation in (22) utilizes the fact that  $R \gg \varepsilon$ . The absolute value of  $\Delta f_D$  should be less than 1/4 to fulfill the imaging accuracy requirement. By substituting (13) into (22), the upper bound of  $u$  is

$$|u| < \frac{2\rho_a}{\sin \beta} \sqrt{\frac{R_c}{\lambda}}. \quad (23)$$

It follows from (14) and (18) that the limitation of the jamming area is

$$|u| < \min \left\{ \frac{\sqrt{R_c} \rho_r}{\sin \beta}, \frac{\sqrt{R_c} \rho_a}{\sin \beta}, \frac{2\rho_a}{\sin \beta} \sqrt{\frac{R_c}{\lambda}} \right\} \quad (24)$$

where  $\min \{ \}$  returns the minimum of the input values.

### III. OPTIMAL RECEIVER LAYOUT

Besides the theory error, the measurement error can neither be ignored in a practical system. This section discusses the effect of the measurement error on the deception jamming inside the theoretical limitation area, and the optimal receiver layout is proposed to reduce its effect. For the synergy netting deception jamming system, the TDOA is usually corrupted by independent and identically distributed (i.i.d.) zero-mean white Gaussian noise, which mainly results from the measurement error. Then, we have that

$$\mathbf{d}_w = \mathbf{Ag} + \mathbf{w} \quad (25)$$

where  $\mathbf{d}_w$  is the TDOA with errors.  $\mathbf{w}$  is an  $n \times 1$  vector with its  $n$ th entry being the measurement error of the  $n$ th receiver. It is zero-mean white Gaussian noise, which is independent among receivers, and we can write  $\mathbf{w} \sim \mathcal{N}(\mathbf{0}, \mathbf{C}_w)$ , with  $\mathbf{C}_w$  being the covariance matrix. As the error of measured TDOA can be modeled as i.i.d. Gaussian noise, we have  $\mathbf{C}_w = \sigma^2 \mathbf{I}$ , where  $\sigma^2$  is the variance of the Gaussian noise. Nevertheless, the linear equations are sensitive to the errors. With an ill conditional  $\mathbf{A}$ , the measurement error will be amplified seriously in the solution  $\mathbf{g}$ . By substituting the entries of  $\mathbf{g}$  into (7), the amplified error is also introduced into the instantaneous range difference  $R_\Delta(t_a)$ . Once the phase error caused by  $R_\Delta(t_a)$  exceeds the range  $[-\pi/4, \pi/4]$ , which is the conventional focusing demanding for SAR imaging, the defocusing occurs to the false scene. The more ill conditional the coefficient matrix  $\mathbf{A}$  is, the less accurate the solution  $\mathbf{g}$  will be under error circumstance, which results in considerable degradation in the performance of the deception jamming.

To tackle this problem, we use the condition number to measure the sensitivity of the linear equations to the errors. The definition of condition number is

$$\kappa(\mathbf{A}) = \|\mathbf{A}^{-1}\| \|\mathbf{A}\| \quad (26)$$

where  $\|\cdot\|$  is any consistent norm, and  $\mathbf{A}$  is assumed to be nonsingular. Here, the norm defined in the square-summable sequence space  $\ell^2$  (denoted by  $\|\cdot\|_2$ ) is used to derive the optimal receiver layout. For any  $\mathbf{A}$ ,  $\kappa(\mathbf{A}) \geq 1$  always holds. The smaller the value of  $\kappa(\mathbf{A})$  is, the less sensitive the solution  $\mathbf{g}$  is to the error perturbation  $\mathbf{w}$ . Therefore, the problem of optimal receiver layout is equivalent to the condition number minimization problem. Considering that  $\mathbf{A}$  is a real matrix,  $\|\mathbf{A}\|_2$  is the positive square root of the maximum eigenvalue of  $\mathbf{A}^T \mathbf{A}$ . The eigenvalues of  $\mathbf{A}^T \mathbf{A}$  are

$$\left\{ \begin{array}{l} \lambda_1 = \frac{1}{2}(-\sqrt{[(x_1 - y_1)^2 + (x_2 + y_1)^2]} \\ \quad \times \sqrt{[(x_1 + y_2)^2 + (x_2 - y_1)^2]} \\ \quad + x_1^2 + x_2^2 + y_1^2 + y_2^2) \\ \lambda_2 = \frac{1}{2}(\sqrt{[(x_1 - y_1)^2 + (x_2 + y_1)^2]} \\ \quad \times \sqrt{[(x_1 + y_2)^2 + (x_2 - y_1)^2]} \\ \quad + x_1^2 + x_2^2 + y_1^2 + y_2^2). \end{array} \right. \quad (27)$$

It is evident that  $\lambda_2 > \lambda_1$ . Moreover, the expression of  $\|\mathbf{A}\|_2$  is shown in (28). After the similar manipulations, we get  $\|\mathbf{A}^{-1}\|_2$  in (29). As a result, the condition number can be calculated by

$$\|\mathbf{A}\|_2 = \sqrt{\lambda_2} = \sqrt{\frac{1}{2}(\sqrt{[(x_1 - y_1)^2 + (x_2 + y_1)^2]}[(x_1 + y_2)^2 + (x_2 - y_1)^2] + x_1^2 + x_2^2 + y_1^2 + y_2^2)} \quad (28)$$

$$\|\mathbf{A}^{-1}\|_2 = \sqrt{\frac{\sqrt{[(x_1 - y_1)^2 + (x_2 + y_1)^2]}[(x_1 + y_2)^2 + (x_2 - y_1)^2] + x_1^2 + x_2^2 + y_1^2 + y_2^2}{2(x_1 y_2 - x_2 y_1)^2}} \quad (29)$$

$$\kappa(\mathbf{A}) = \|\mathbf{A}^{-1}\|_2 \|\mathbf{A}\|_2 = \frac{\sqrt{[(x_1 - y_1)^2 + (x_2 + y_1)^2]}[(x_1 + y_2)^2 + (x_2 - y_1)^2] + x_1^2 + x_2^2 + y_1^2 + y_2^2}{2|x_1 y_2 - x_2 y_1|}. \quad (30)$$

(30). Here, the  $|\cdot|$  denotes the absolute value. Eqn(28)–(30) as shown at the bottom of the page.

For simplicity of notation, vectors are used to denote the coordinates of the receivers. Let  $\mathbf{a}_1 = (x_1, y_1, 0)$ ,  $\mathbf{a}_2 = (x_2, y_2, 0)$ ,  $\mathbf{a}'_2 = (y_2, -x_2, 0)$ , and  $\mathbf{a}''_2 = (-y_2, x_2, 0)$ . Noticing that  $\mathbf{a}_2 \perp \mathbf{a}'_2$  and  $\mathbf{a}_2 \perp \mathbf{a}''_2$ , it follows from (30) that

$$\kappa(\mathbf{A}) = \frac{\|\mathbf{a}_1 - \mathbf{a}'_2\|_2 \|\mathbf{a}_1 - \mathbf{a}''_2\|_2 + \|\mathbf{a}_1\|_2^2 + \|\mathbf{a}_2\|_2^2}{2|\langle \mathbf{a}_1, \mathbf{a}'_2 \rangle|}. \quad (31)$$

Recall that the  $\ell^2$  norm of a vector is the length of the vector. According to the geometry of the synergy netting deception jamming system, we get the following constraints of optimal receiver layout design.

- 1) Neither of the two receivers is superposed on the jammer. Therefore, we have  $\mathbf{a}_1 \neq \mathbf{0}$  and  $\mathbf{a}_2 \neq \mathbf{0}$ .
- 2) As  $\|\mathbf{a}_1 - \mathbf{a}'_2\|_2 \geq 0$  and  $\|\mathbf{a}_1 - \mathbf{a}''_2\|_2 \geq 0$ , we obtain  $\|\mathbf{a}_1 - \mathbf{a}'_2\|_2 \|\mathbf{a}_1 - \mathbf{a}''_2\|_2 \geq 0$ .
- 3) It is easy to obtain  $|\langle \mathbf{a}_1, \mathbf{a}'_2 \rangle| \geq 0$ . Actually, the jammer is usually not collinear with the receivers, leading to  $|\langle \mathbf{a}_1, \mathbf{a}'_2 \rangle| > 0$ . This constraint is in line with the non-singular condition of  $\mathbf{A}$ .

Therefore, the optimal layout can be formulated as

$$\begin{aligned} \min \quad & \kappa(\mathbf{A}) \\ \text{s. t.} \quad & (x_n, y_n, 0) \neq (0, 0, 0) \\ & (x_n, y_n, 0) \neq q(x_m, y_m, 0) \\ & (x_n, y_n, 0) \neq q(-x_m, -y_m, 0) \\ & \sqrt{x_n^2 + y_n^2} \leq r \end{aligned} \quad (32)$$

where  $m, n = 1, 2$ ,  $q \in \mathbb{R}^+$  is the proportionally coefficient. The last constraint guarantees that the receivers are within a circular region with the jammer being the center and  $r$  being radius.

To minimize  $\kappa(\mathbf{A})$ , we need to maximize the denominator and minimize the numerator of (31). Denoting the angle between  $\mathbf{a}_1$  and  $\mathbf{a}_2$  by  $\Phi$ , thus the angle between  $\mathbf{a}_1$  and  $\mathbf{a}'_2$  is  $\Phi - 90^\circ$ . Then, the denominator can be expressed by

$$\begin{aligned} |\mathbf{a}_1 \cdot \mathbf{a}'_2| &= \|\mathbf{a}_1\|_2 \|\mathbf{a}'_2\|_2 \cos(\Phi - 90^\circ) \\ &= \|\mathbf{a}_1\|_2 \|\mathbf{a}'_2\|_2 |\sin \Phi| \\ &\leq \|\mathbf{a}_1\|_2 \|\mathbf{a}'_2\|_2. \end{aligned} \quad (33)$$

The maximum of (33) can be obtained when  $|\sin \Phi| = 1$ , meaning that  $\Phi = 90^\circ$  or  $\Phi = 270^\circ$ . Therefore, the denominator is maximized provided that  $\mathbf{a}_1 \perp \mathbf{a}_2$ . Let us now consider

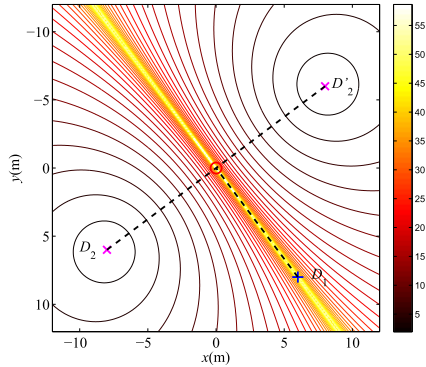


Fig. 3. Optimal layout of receivers.

the numerator of (31). Let  $\mathbf{a}_1 = (r_1 \cos \phi_1, r_1 \sin \phi_1, 0)$ ,  $\mathbf{a}'_2 = (r_2 \cos \phi_2, r_2 \sin \phi_2, 0)$ ,  $\mathbf{a}''_2 = (-r_2 \cos \phi_2, -r_2 \sin \phi_2, 0)$ , where  $r_1 = \|\mathbf{a}_1\|_2$ ,  $\phi_1 = \arctan(y_1/x_1)$ ,  $r_2 = \|\mathbf{a}_2\|_2$ ,  $\phi_2 = -\arctan(x_2/y_2)$ . Then, the numerator can be rewritten as

$$\begin{aligned} & \|\mathbf{a}_1 - \mathbf{a}_2'\|_2 \|\mathbf{a}_1 - \mathbf{a}_2''\|_2 + \|\mathbf{a}_1\|_2^2 + \|\mathbf{a}_2\|_2^2 \\ &= \sqrt{(r_1^2 + r_2^2)^2 - 4r_1^2 r_2^2 \cos^2(\phi_1 - \phi_2)} + r_1^2 + r_2^2 \\ &\geq \sqrt{(r_1^2 + r_2^2)^2 - 4r_1^2 r_2^2} + r_1^2 + r_2^2 \\ &= |r_1^2 - r_2^2| + r_1^2 + r_2^2 \\ &= \|\mathbf{a}_1\|_2^2 - \|\mathbf{a}_2\|_2^2 + \|\mathbf{a}_1\|_2^2 + \|\mathbf{a}_2\|_2^2. \end{aligned} \quad (34)$$

The minimum of (34) is obtained when  $\phi_1 = \phi_2$  or  $\phi_1 - \phi_2 = 180^\circ$ . Recalling that  $\mathbf{a}_2 \perp \mathbf{a}'_2$ , the minimum of the numerator can be attained provided that  $\mathbf{a}_1 \perp \mathbf{a}_2$ , which also lead to the maximum of the denominator. Thus, the numerator minimization and the denominator maximization are fulfilled simultaneously.

Using the orthogonality  $\mathbf{a}_1 \perp \mathbf{a}_2$ , we have

$$\kappa(\mathbf{A}) = \frac{\|\mathbf{a}_1\|_2^2 - \|\mathbf{a}_2\|_2^2 + \|\mathbf{a}_1\|_2^2 + \|\mathbf{a}_2\|_2^2}{2\|\mathbf{a}_1\|_2\|\mathbf{a}'_2\|_2} \quad (35)$$

which can be further simplified as

$$\kappa(\mathbf{A}) = \begin{cases} \frac{\|\mathbf{a}_1\|_2}{\|\mathbf{a}_2\|_2} > 1, & \|\mathbf{a}_1\|_2 > \|\mathbf{a}_2\|_2 \\ \frac{\|\mathbf{a}_1\|_2^2 + \|\mathbf{a}_2\|_2^2}{2\|\mathbf{a}_1\|_2\|\mathbf{a}_2\|_2} = 1, & \|\mathbf{a}_1\|_2 = \|\mathbf{a}_2\|_2 \\ \frac{\|\mathbf{a}_2\|_2}{\|\mathbf{a}_1\|_2} > 1, & \|\mathbf{a}_1\|_2 < \|\mathbf{a}_2\|_2. \end{cases} \quad (36)$$

This indicates that the minimum value of  $\kappa(\mathbf{A})$  is achieved when  $\|\mathbf{a}_1\|_2 = \|\mathbf{a}_2\|_2$ . With the orthogonal condition  $\mathbf{a}_1 \perp \mathbf{a}_2$ , the optimal layout of the jammer and receivers is a isosceles right triangle with the jammer being the right-angle vertex.

Fig. 3 shows the contour lines of the condition numbers of different receiver layouts. Different colors of the contour lines denote the condition number of different layouts, as the color bar shows. The jammer locates at the origin, which is marked by “o.” Receiver  $D_1$  is fixed at an arbitrary location, say, (6, 8, 0) m, denoted by “+.” By moving receiver  $D_2$  along the

horizontal plane, we get the minimum condition number when  $D_2$  locates at the places marked by “x”’s in Fig. 3. This verifies the optimal layout derivation. The optimal layout leads to the least system sensitivity to the TDOA measurement error because of the smallest condition number of  $\mathbf{A}$ .

Note that the coefficient matrix  $\mathbf{A}$  is independent of the SAR kinematic parameters. Therefore, the deception jamming system has the similar performance against SAR heading in different directions and with different beam pointing. Thus, the optimal layout is universal for different SAR kinematic parameters and mainly determined by the right angle relationship between  $\mathbf{a}_1$  and  $\mathbf{a}_2$ , regardless of the value of  $\phi_1$ .

#### IV. ERROR LIMITATION ANALYSIS

##### A. Performance of Optimal Layout Under Error Circumstances

According to Section III, once one of the receivers, say,  $D_1$ , is deployed at  $(x_1, y_1, 0)$ , there are two possible optimal locations  $((y_1, -x_1, 0)$  and  $(-y_1, x_1, 0)$ ) for the second receiver  $D_2$  to choose from. By minimizing the condition number of  $\mathbf{A}$ , these locations lead to the similar performance under the same error level. Here, we take  $(y_1, -x_1, 0)$  as the location of receiver  $D_2$  for further analysis.

The linear least-square (LLS) cost function is

$$J(\mathbf{g}) = (\mathbf{Ag} - \mathbf{d}_w)^T (\mathbf{Ag} - \mathbf{d}_w) \quad (37)$$

which, when minimized, leads to the estimation of  $\mathbf{g}$ , given as

$$\hat{\mathbf{g}} = \mathbf{A}^{-1} \mathbf{d}_w. \quad (38)$$

The bias and mean square error (MSE) of  $\hat{\mathbf{g}}$  are, respectively, calculated as

$$\text{bias}(\hat{\mathbf{g}}) = -\frac{E\{J'(\mathbf{g})\}}{E\{J''(\mathbf{g})\}} = -\frac{E\{\mathbf{A}^T \mathbf{w}\}}{\mathbf{A}^T \mathbf{A}} = 0 \quad (39)$$

$$\text{MSE}(\hat{\mathbf{g}}) = \frac{E\{(J'(\mathbf{g}))^2\}}{(E\{J''(\mathbf{g})\})^2} = \frac{E\{\mathbf{w}^T \mathbf{A} \mathbf{A}^T \mathbf{w}\}}{(\mathbf{A}^T \mathbf{A})^T (\mathbf{A}^T \mathbf{A})}. \quad (40)$$

Since  $\text{bias}(\hat{\mathbf{g}}) = 0$ , LLS is an unbiased estimator, which means that its MSE equals the variance  $\mathbf{C}_{\hat{\mathbf{g}}}$ . Substituting the coordinates of  $D_1$  and  $D_2$  into (40), we obtain

$$\mathbf{C}_{\hat{\mathbf{g}}} = \frac{1}{r_1^2} \mathbf{C}_w = \frac{\sigma^2}{r_1^2} \mathbf{I}. \quad (41)$$

Meanwhile, inserting the coordinates of the false scatterer  $F$  and the estimates  $\hat{g}_x(t_a)$  and  $\hat{g}_y(t_a)$  into (7), we can obtain the estimation of the instantaneous slant range difference, i.e.,  $\hat{R}_{\Delta F}(t_a)$ . The mean and variance of  $\hat{R}_{\Delta F}(t_a)$  are

$$E\{\hat{R}_{\Delta F}\} = x_F \hat{g}_x(t_a) + y_F \hat{g}_y(t_a) = R_{\Delta F}(t_a) \quad (42)$$

$$\begin{aligned} & E\{(\hat{R}_{\Delta F}(t_a) - E\{\hat{R}_{\Delta F}(t_a)\})^2\} \\ &= E\{[(x_F \hat{g}_x(t_a) + y_F \hat{g}_y(t_a)) - (x_F g_x(t_a) + y_F g_y(t_a))]^2\} \\ &= E\{x_F^2 (\hat{g}_x(t_a) - g_x(t_a))^2 + y_F^2 (\hat{g}_y(t_a) - g_y(t_a))^2\} \\ &= \sigma^2 r_F^2 / r_1^2. \end{aligned} \quad (43)$$

Therefore, the synergy netting deception jamming system is an unbiased estimator of the instantaneous slant range

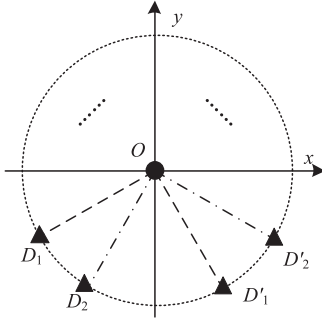


Fig. 4. Collaborative receivers' layout.

difference. Moreover,  $\hat{R}_{\Delta F}(t_a)$  is Gaussian distributed, namely,  $\hat{R}_{\Delta F}(t_a) \sim \mathcal{N}(R_{\Delta F}(t_a), \sigma^2 r_F^2/r_1^2)$ . That is to say, once the layout of the jamming system is fixed (say,  $r_1$  is a constant), the performance of the estimator is only affected by the distance between the false scatterer and jammer, which verifies the universality of the optimal layout against different SAR kinematic parameters.

### B. Collaborative Deception Jamming

To further reduce the effect of the errors on the solved coefficients, collaborative receivers are introduced. Assuming that  $M$  receivers are involved, (8) can be reorganized as a set of overdetermined linear equations

$$\begin{pmatrix} x_1 & y_1 \\ x_2 & y_2 \\ \vdots & \vdots \\ x_m & y_m \\ \vdots & \vdots \\ x_M & y_M \end{pmatrix} \begin{pmatrix} g_x(t_a) \\ g_y(t_a) \end{pmatrix} = \begin{pmatrix} R_{\Delta 1}(t_a) \\ R_{\Delta 2}(t_a) \\ \vdots \\ R_{\Delta m}(t_a) \\ \vdots \\ R_{\Delta M}(t_a) \end{pmatrix}. \quad (44)$$

The cooperative receivers are able to provide more observations of TDOAs, with which the LLS estimator can be performed. The overdetermined linear equations with errors in matrix form are  $\mathbf{d}_{wc} = \mathbf{A}_c \mathbf{g} + \mathbf{w}_c$ . Then, the unique LLS estimation of the coefficients can be calculated by

$$\hat{\mathbf{g}}_{lls} = (\mathbf{A}_c^T \mathbf{A}_c)^{-1} \mathbf{A}_c^T \mathbf{d}_{wc}. \quad (45)$$

To suppress the errors, the condition number of  $\mathbf{A}_c$  should also be minimized, leading to the optimal layout for the collaborative receivers. In doing so, we herein propose one feasible scheme employing the optimal layout deduced in Section III as a basic module. The collaborative deception jamming system can be expanded by simultaneously adding two receivers, which constructs a isosceles right triangle together with the jammer, as a module. The collaborative deception jamming system is shown in Fig. 4.

Receivers  $D_1$  and  $D'_1$  are deployed following the optimal layout as a module. Receivers  $D_2$  and  $D'_2$  are added as another module. Therefore, the number of receivers are even. More modules

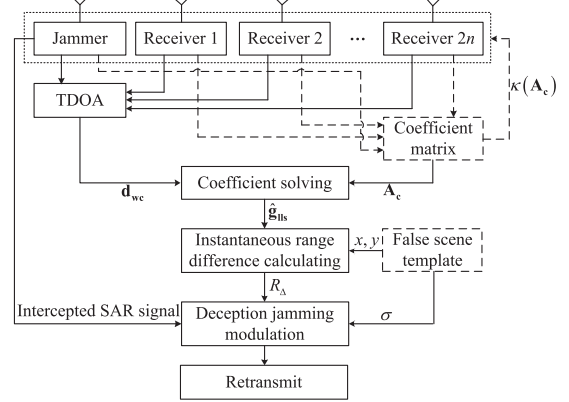


Fig. 5. System working flowchart.

can be introduced into the collaborative deception jamming system so that the performance of the error suppression can be enhanced. Note that neither of two receivers is collinear with the jammer. The locations of collaborative receivers in Fig. 4 ensure that the condition number of  $\mathbf{A}_c$  equals 1, which is proved in the Appendix.

### C. System Working Flowchart

Basing on the analysis above, the working flowchart of the proposed deception jamming scheme is given in Fig. 5.

Considering the unavoidable measurement errors,  $2n$  collaborative receivers, which intercept the SAR signal together with the jammer, are involved in the jamming system. The locations of the receivers are first gathered to calculate the coefficient matrix  $\mathbf{A}_c$ . Then, the condition number  $\kappa(\mathbf{A}_c)$  is fed back to adjust the receivers locations to obtain the optimal system performance on measurement errors. This procedure is illustrated with dashed lines to show that they can be carried out before the jamming starts.

When performing deception jamming, the TDOAs between the receivers and jammer are collected into a vector  $\mathbf{d}_{wc}$ . Subsequently,  $\mathbf{d}_{wc}$  and  $\mathbf{A}_c$  are substituted into (38) to estimate the jamming modulation coefficients. On the other hand, the instantaneous range difference  $R_\Delta$  can be calculated utilizing the coordinates of each false scatterer. The template of false scene can also be designed in advance. Finally, the intercepted SAR signal is modulated according to the scattering coefficient and instantaneous range difference of each false scatterer, and then retransmitted to the SAR.

## V. SIMULATION RESULTS

### A. Scatterers Simulation

In this simulation, the netting deception jamming is performed in the ideal situation with only far-field approximation error to verify the theoretical accuracy. Without measurement error, the netting deception jamming has the same performance with different receivers' layout. Therefore, the receivers are set at arbitrary coordinates, say,  $(6, 8, 0)$  and  $(-6.4, 7.7, 0)$  m, for

TABLE I  
SAR PARAMETERS

| Parameter               | Symbol     | Value                   |
|-------------------------|------------|-------------------------|
| Bandwidth               | $B_r$      | 50 MHz                  |
| Pulse Width             | $T_p$      | 1 $\mu$ s               |
| Chirp Rate              | $\gamma$   | $5 \times 10^{13}$ Hz/s |
| Wavelength              | $\lambda$  | 0.033 m                 |
| Carrier Frequency       | $f_c$      | 9 GHz                   |
| Aperture Length         | $D_a$      | 6 m                     |
| Beamwidth               | $\Theta_a$ | 0.0056 rad              |
| Closest Range           | $R_s$      | 800 km                  |
| Speed                   | $v$        | 7000 m/s                |
| Squint Angle            | $\theta_c$ | 10°                     |
| Grazing Angle           | $\beta_c$  | 20°                     |
| Doppler Bandwidth       | $B_a$      | 2339.7 Hz               |
| Synthetic Aperture Time | $T_a$      | 0.65 s                  |

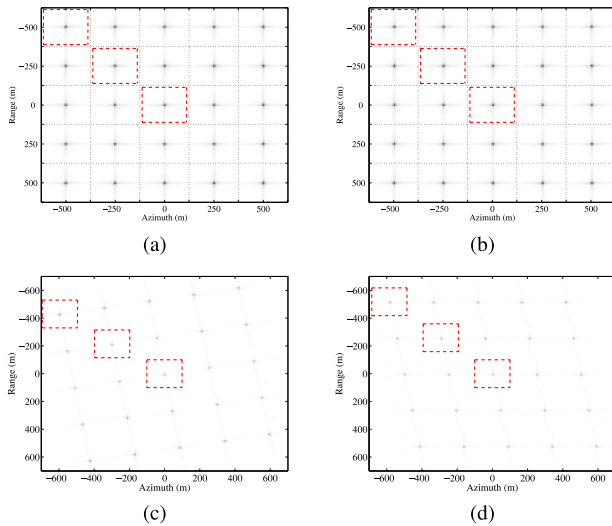


Fig. 6. Imaging results of the real and false scenes. (a) Real scene. (b) False scene. (c) False scene generated using algorithm in [21]. (d) False scene generated using algorithm in [22].

example, in the simulation. A spaceborne SAR platform working in strip map mode is set up in the simulation, of which parameters are listed in Table I. According to the analysis in Section II-B, the jamming area is  $\pm 4.53$  km width, while the jamming area of the conventional scheme is only  $\pm 540$  m [21]. The simulation scene is set in the feasible area, where the netting deception jamming works. The scatterers are set as a  $5 \times 5$  array centered at the origin with 250-m separation between neighbouring scatterers. The false scatterers in the jamming scene are the same as those in the real scene for the purpose of comparison.

To show the imaging result clearly, the blank gaps between scatterers are removed. Square areas, whose sides being 100 m, around scatterers are selected and rearranged together in the imaging results, as illustrated in Fig. 6 (a). The jamming result obtained using the proposed algorithm is plotted in Fig. 6(b). Being discussed in the ground coordinates, the proposed algorithm is able to tackle the geometric distortion without coordinate transformation. Fig. 6(c) and (d) shows the jamming result using the conventional algorithms described in [21] and [22],

respectively. Both the algorithms are discussed in the imaging plane; therefore, the false targets generated by the conventional methods suffer geometric distortion caused by squint imaging mode. Notice that the approach in [21] is designed for side-look SAR working mode. Therefore, the false targets distort worse than those obtained using the algorithm in [22], which is devised for squint SAR.

For ease of description, the real scatterers are mentioned by  $P_{k,l}$ , while the false scatterers are mentioned by  $F_{k,l}$ . The  $k$  and  $l$  denote the row and column indexes of the scatterer in the array, respectively. The false scatterers obtained using the conventional methods suggested in [21] and [22] are denoted by  $Q'_{k,l}$  and  $Q''_{k,l}$ , respectively. We take scatterers with  $(k, l) \in \{(1, 1), (2, 2), (3, 3)\}$ , which are surrounded by the dashed lines in Fig. 6, for further analysis. The partial enlarged details are depicted in Fig. 7.

The centers of the real scatterers are marked by “+” in all the images in Fig. 7, which provides reference positions for the false scatterers positional transposition evaluation. Notice that the false scatterers in Fig. 7(d) and (e) slightly transpose from the real ones. This is caused by the approximation of the far-field assumption, which introduces error in (6) by ignoring the high-order terms of  $x_p$  and  $y_p$  [23]. The effect of the approximation error can be ignored when the transposition is less than half of one resolution cell. The false scatterers  $F_{3,3}$ ,  $Q'_{3,3}$ , and  $Q''_{3,3}$ , which are shown in Fig. 7(f), (i), and (l), respectively, do not transpose from the real one due to their zero coordinates. The false scatterers yielded by the conventional schemes become worse as their distances from the jammer increase, as demonstrated in Fig. 7(g), (h), (j), and (k). Without considering the squint imaging parameters,  $Q'_{1,1}$  and  $Q'_{2,2}$  defocus more seriously than  $Q''_{2,2}$  and  $Q''_{2,2}$ . To analyze the quality of deception jamming quantitatively, the normalized sectional plots of the real and false scatterers in azimuth are plotted in Fig. 8, and the evaluation indexes are listed in Table II.

In Fig. 8, the solid lines are the sectional plots of the real scatterers, and the lines marked by “○,” “□,” and “△” are the false scatterers  $F$ ,  $Q'$ , and  $Q''$ . Ignoring the azimuth positional errors, sectional plots of  $Q'$  and  $Q''$  are aligned with the others for comparison. They are nearly superposed on each other. The impulse response width (IRW), peak side-lobe ratio (PSLR), and integrated side-lobe ratio (ISLR) of the false scatterers are nearly equal to those of the real ones, which means that the deception jamming algorithm is able to achieve the similar imaging quality as the real scene. Furthermore, the positional errors of the false scatterers in both range and azimuth are less than half of one resolution cell. The evaluation indexes of  $Q'$  and  $Q''$  describe the defocusing and geometric distortions quantitatively, which show the limitation of the conventional method in complex SAR imaging mode.

## B. Error Amplification Effect Versus Condition Number

1) Two-Receiver Deception Jamming With Different Condition Numbers: As stated above, the measurement errors are unavoidable and will be amplified by the linear equations, leading to random envelop shift and phase decoherence, which

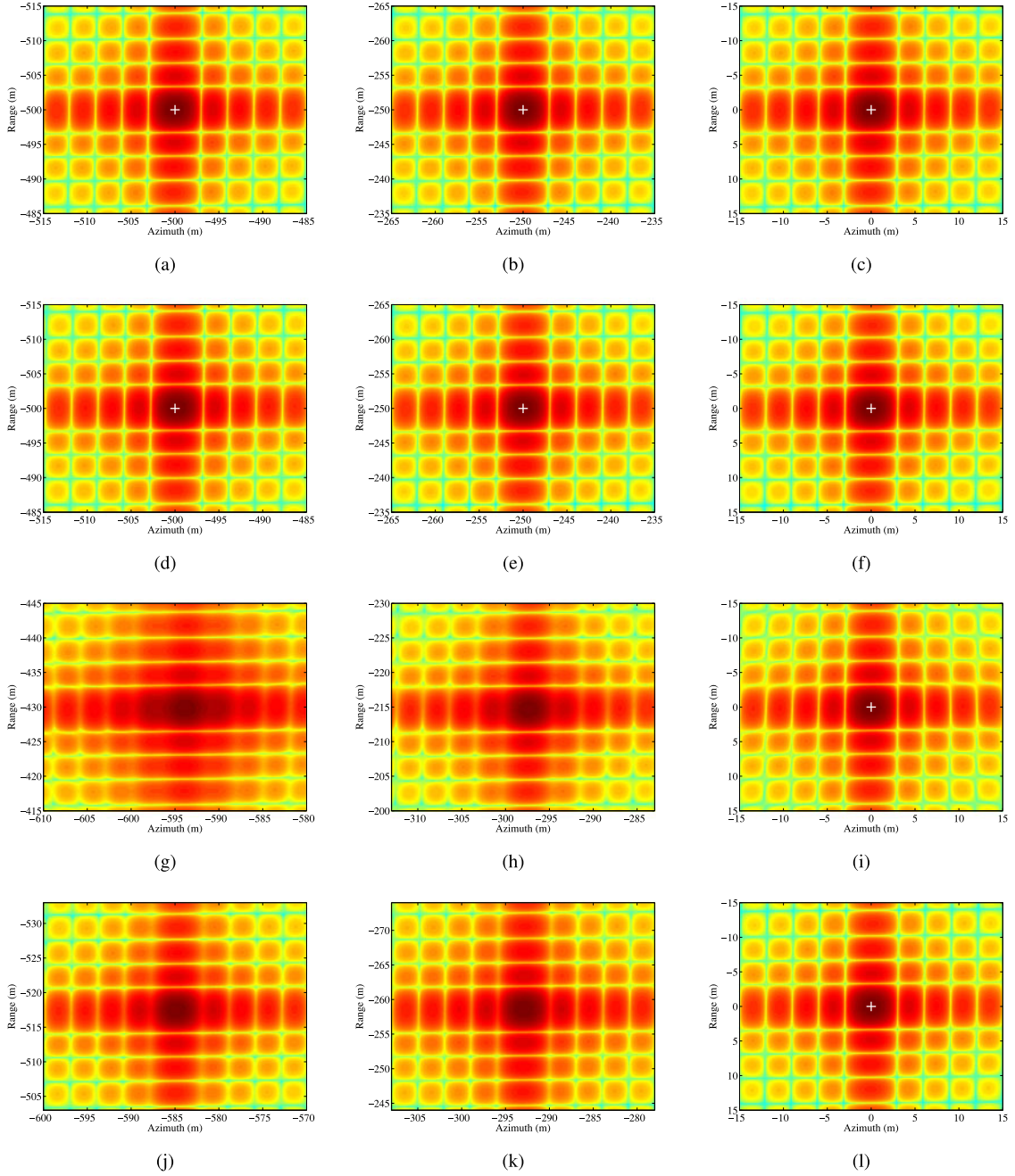


Fig. 7. Imaging and deception jamming results of scatterers. (a) Real scatterer  $P_{1,1}$ . (b) Real scatterer  $P_{2,2}$ . (c) Real scatterer  $P_{3,3}$ . (d) False scatterer  $F_{1,1}$ . (e) False scatterer  $F_{2,2}$ . (f) False scatterer  $F_{3,3}$ . (g) False scatterer  $Q'_{1,1}$ . (h) False scatterer  $Q'_{2,2}$ . (i) False scatterer  $Q'_{3,3}$ . (j) False scatterer  $Q''_{1,1}$ . (k) False scatterer  $Q''_{2,2}$ . (l) False scatterer  $Q''_{3,3}$ .

eventually degrades the imaging performance of the deception jamming. To evaluate the amplification effect of the linear equations for error, two-receiver layouts with different condition numbers, as illustrated in Fig. 9, are simulated.

Fig. 9 shows the condition number curve obtained with receivers distributed on the circle with radius  $r = 10$  m. The marks in this figure are the same as those in Fig. 3. With receiver  $D_1$  being fixed at  $(6, 8, 0)$  m, three locations for another receiver, which are labeled by  $D_2(-8, 6, 0)$ ,  $D_{21}(-10, 0.03, 0)$ , and  $D_{22}(-9.60, -2.80, 0)$  m, are set for simulations. Their

condition numbers equal 1, 2, and 3, respectively. Denote the false scatter obtained using two receivers by  $F'_{k,l}$ . To show the amplification effect of the linear equations for error, a contrast false scatterer  $F'_{2,2}$ , for whom the error is directly introduced into the calculated jamming modulation coefficient rather than the coefficient matrix of the linear equations, is also simulated.

According to the literature [24]–[26], the accuracy of TDOA measurements is around 1 ps, which corresponds to the accuracy of the slant range difference measurement, i.e.,  $1.5 \times 10^{-4}$  m. Therefore, we model the measurement error of  $R_{\Delta m}(t_a)$  as

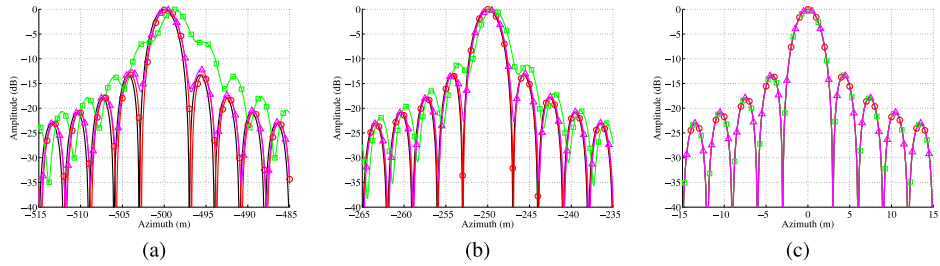


Fig. 8. Normalized sectional plots of the imaging and deception jamming results. (a) Sectional plots of  $P_{1,1}$ ,  $F_{1,1}$ ,  $Q'_{1,1}$  and  $Q''_{1,1}$ . (b) Sectional plots of  $P_{2,2}$ ,  $F_{2,2}$ ,  $Q'_{2,2}$  and  $Q''_{2,2}$ . (c) Sectional plots of  $P_{3,3}$ ,  $F_{3,3}$ ,  $Q'_{3,3}$  and  $Q''_{3,3}$ .

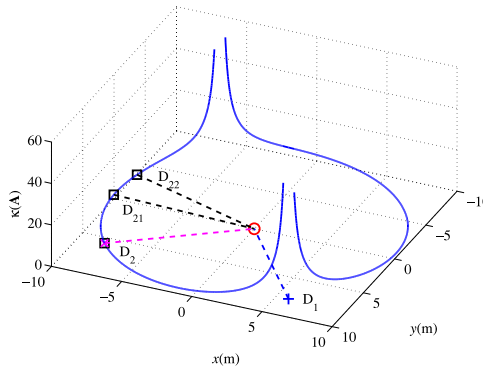


Fig. 9. Condition number variation on a circular region.

TABLE II

DECEPTION JAMMING QUALITY INDEXES OF THE SYNERGY NETTING DECEPTION JAMMING ALGORITHM WITHOUT MEASUREMENT ERROR

|             | IRW(m) | PSLR(dB) | ISLR(dB) | Range positional error(m) | Azimuth positional error(m) |
|-------------|--------|----------|----------|---------------------------|-----------------------------|
| $P_{1,1}$   | 2.66   | -13.27   | -10.42   | —                         | —                           |
| $F_{1,1}$   | 2.66   | -13.27   | -10.43   | 0.10                      | -0.25                       |
| $Q'_{1,1}$  | 2.99   | -6.65    | -4.83    | 70.10                     | -93.80                      |
| $Q''_{1,1}$ | 2.69   | -12.23   | -9.34    | -17.90                    | -84.75                      |
| $P_{2,2}$   | 2.66   | -13.27   | -10.42   | —                         | —                           |
| $F_{2,2}$   | 2.66   | -13.26   | -10.42   | 0.05                      | -0.05                       |
| $Q'_{2,2}$  | 2.73   | -11.03   | -8.33    | 35.25                     | -47.35                      |
| $Q''_{2,2}$ | 2.67   | -12.99   | -10.13   | -9.35                     | -42.85                      |
| $P_{3,3}$   | 2.66   | -13.27   | -10.42   | —                         | —                           |
| $F_{3,3}$   | 2.66   | -13.27   | -10.42   | 0.00                      | 0.00                        |
| $Q'_{3,3}$  | 2.66   | -13.24   | -10.43   | 0.00                      | 0.00                        |
| $Q''_{3,3}$ | 2.66   | -13.27   | -10.42   | 0.00                      | 0.00                        |

the zero-mean Gaussian noise with its standard deviation being  $1.5 \times 10^{-4}$  m. Deception jamming of false scatterer  $F'_{2,2}$  is simulated under the same error level for different receiver layouts. The imaging results of false scatterer  $F'_{2,2}$  are given in Fig. 10.

When being added to the modulation coefficient directly, this level of error has little effect on the deception jamming result. Therefore, the contrast false scatterer  $F'_{2,2}$  in Fig. 10(a), which is obtained by directly adding the same error level to the jamming coefficients, is nearly the same as the false scatterer obtained with accurate modulation coefficient given in Fig. 7(e). When showing up in the linear equations, the error is amplified to

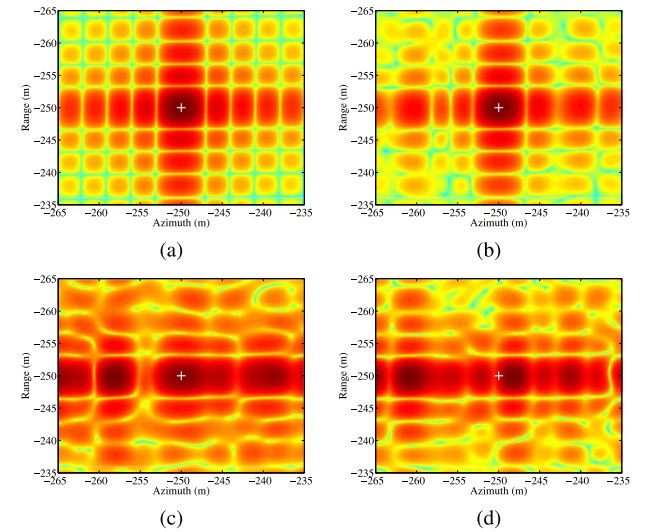
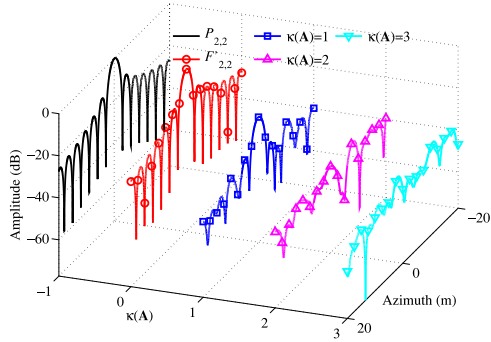
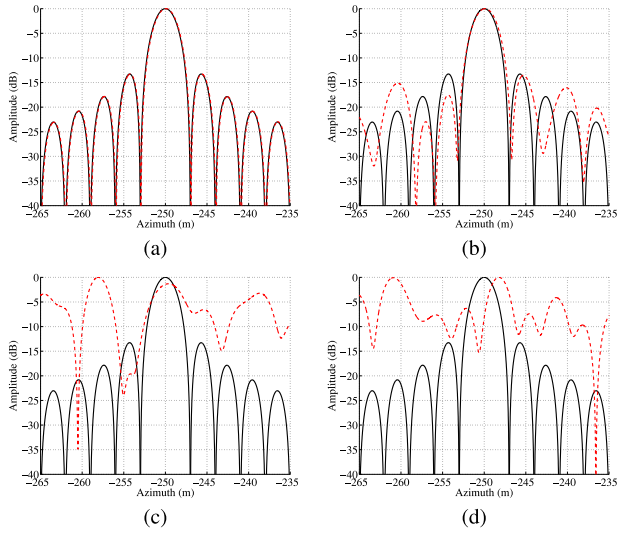


Fig. 10. Deception jamming results of scatterers versus condition number. (a) Contrast false scatterer  $F'_{2,2}$ . (b)  $\kappa(\mathbf{A}) = 1$ . (c)  $\kappa(\mathbf{A}) = 2$ . (d)  $\kappa(\mathbf{A}) = 3$ .

lower the imaging quality of deception jamming. The effect of errors on deception jamming mainly shows up as defocus in azimuth. When  $\kappa(\mathbf{A}) = 1$ , the main lobe of false scatterer  $F'_{2,2}$  in azimuth can still be guaranteed under error circumstances as Fig. 10(b) shows. But its side lobes are not ideally symmetrical due to the disturbance of error. With the increase of condition number of the deception jamming system, the side lobes of the false scatterer becomes worse, which even bury the main lobe, as shown in Fig. 10(c) and (d). At the same time, the amplitude of the main lobe reduces quickly with the condition number increasing, as shown in Fig. 11.

The solid line in Fig. 11 is the sectional plot of the real scatterer  $P_{2,2}$ , which is considered as a reference. The contrast false scatterer  $F'_{2,2}$ , whose sectional plot is marked by “○,” approaches the imaging quality of  $P_{2,2}$ . The sectional plots with condition numbers equal 1, 2, and 3 are marked by “□,” “△,” and “▽,” respectively. The main lobe of the false scatterer obtained with  $\kappa(\mathbf{A}) = 1$  reduces by 17.77 dB, which makes it much weaker than the real one. However, the shape of the Sinc function can still be vaguely recognized. As the condition numbers increase to 2 and 3, the main lobes of the false scatterers reduce to -34.76 and -33.78 dB, respectively. They are far lower than the side lobe of the real scatterer, which means that the deception

Fig. 11. Sectional plots of false scatterers  $F'_{2,2}$  versus condition number.Fig. 12. Normalized sectional plots of the deception jamming results versus condition number. (a) Contrast false scatterer  $F'_{2,2}$ . (b)  $\kappa(\mathbf{A}) = 1$ . (c)  $\kappa(\mathbf{A}) = 2$ . (d)  $\kappa(\mathbf{A}) = 3$ .

jamming will be buried by the real scene. The normalized sectional plots are given in Fig. 12 for further quantitative evaluation.

In Fig. 12(a), the sectional plot of the contract false scatterer  $F'_{2,2}$  (dashed line) is almost superposed on that of the real scatterer  $P_{2,2}$  (solid line). The error does not reduce the deception jamming quality significantly. When being amplified by the linear equations, the error leads to the rise of side lobe level for the false scatterer as shown in Fig. 12(b), even though the optimal layout for receivers is employed. As the condition number increases, it becomes more difficult for the false scatterer to be coherently accumulated in azimuth. In Fig. 12(c) and (d), the sectional plots of the false scatterer get worse and the side lobes rise to the level of main lobe. The evaluation indexes are listed in Table III.

The PSLR of the contract false scatterer  $F'_{2,2}$  increases by 0.08% compared with the false scatterer  $F_{2,2}$  obtained utilizing the accurate coefficients. The other indexes of  $F'_{2,2}$  are equal to those of  $F_{2,2}$ . The amplification of error expands the main lobe of the false scatterer and lead to energy leakage to the side lobes.

TABLE III  
DECEPTION JAMMING QUALITY INDEXES WITH MEASUREMENT ERROR OF SCATTERER  $F_{2,2}$  VERSUS CONDITION NUMBER

|                          | IRW(m) | PSLR(dB) | ISLR(dB) | Range positional error(m) | Azimuth positional error(m) |
|--------------------------|--------|----------|----------|---------------------------|-----------------------------|
| $F'_{2,2}$               | 2.66   | -13.25   | -10.42   | 0.05                      | -0.05                       |
| $\kappa(\mathbf{A}) = 1$ | 2.81   | -13.54   | -9.84    | 0.05                      | -0.15                       |
| $\kappa(\mathbf{A}) = 2$ | 2.83   | -1.30    | 5.29     | -0.15                     | 8.05                        |
| $\kappa(\mathbf{A}) = 3$ | 2.30   | -0.07    | 5.11     | -0.05                     | -1.75                       |

When  $\kappa(\mathbf{A}) = 1$ , the IRW and ISLR of the false scatterer increase by 5.64% and 5.57%, and the PSLR decreases by 2.19%. Therefore, the imaging result of the false scatterer can be generally guaranteed. As the condition number increases, the PSLR of the false scatterer increases nearly to zero, which means that it is difficult to distinguish the main lobe from side lobes. Thus, the other evaluation indexes become meaningless. The simulation results verify the amplification effect of the linear equations and show the necessity of receiver layout optimization.

2) *Collaborative Deception Jamming With Different Condition Numbers:* Although the LLS estimator given in (45) is able to eliminate error, the error suppression performance is limited if the receivers are not well organized. Therefore, condition number minimization is also necessary for collaborative deception jamming. In this simulation, collaborative deception jamming results with different condition numbers are given to confirm this statement. In particular, 24 receivers are used in the simulation with different layouts, whose condition numbers are 1, 2, and 3, respectively. The false scatterers obtained are denoted by  $F''_{k,l}$ . Since the LLS estimator is able to suppress the error, the false scatterer  $F''_{2,2}$  is generally focused. Therefore, the false scatterer  $F''_{1,1}$ , which lies farther away from the jammer and is much easier effected by the error, is analyzed in this simulation.

The collaborative receivers perform as the LLS estimator on measurement error. As a result, the false scatterers can be generally focused. Fig. 13 (a) shows the imaging result of the false scatterer  $F''_{1,1}$  obtained without measurement error for contrast. The imaging result in Fig. 13(b) is obtained with  $\kappa(\mathbf{A}) = 1$ . The measurement error can be effectively eliminated by the LLS estimator utilizing collaborative receivers, which guarantees the imaging quality. As the condition number increases, the side lobe of the false scatterer gets worse, as indicated in Fig. 13(c) and (d). Sectional plots of  $F''_{1,1}$  with different condition numbers are given in Fig. 14 to show the main lobe amplitude loss.

For different condition numbers equaling 1, 2, and 3, the amplitudes of the main lobes reduce to -5.71, -9.82, and -17.45 dB, respectively. Compared to the jamming result obtained with two receivers, the collaborative jamming method accumulates more energy into the main lobe. To further analyze the other imaging quality quantificationally, the normalized sectional plots are given in Fig. 15, and the evaluation indexes are listed in Table IV.

The evaluation indexes of false scatterers obtained when  $\kappa(\mathbf{A}) = 1$  and  $\kappa(\mathbf{A}) = 2$  do not deviate far from that of the contract scatterer  $F''_{1,1}$ . Therefore, the imaging result can still

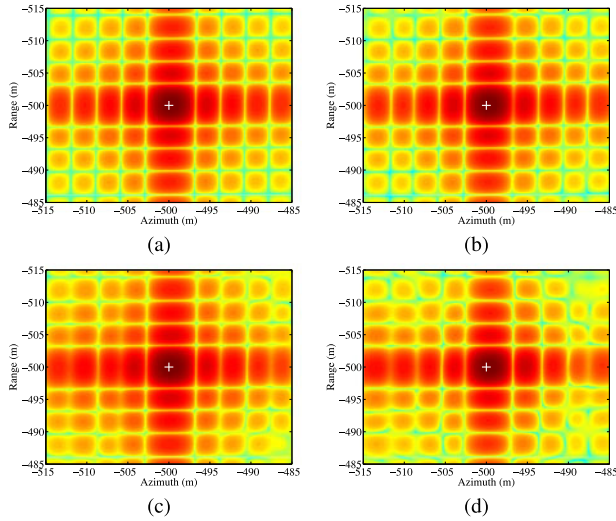


Fig. 13. Collaborative deception jamming results of scatterers versus condition number. (a) Contrast false scatterer  $F''_{1,1}$ . (b)  $\kappa(\mathbf{A}) = 1$ . (c)  $\kappa(\mathbf{A}) = 2$ . (d)  $\kappa(\mathbf{A}) = 3$ .

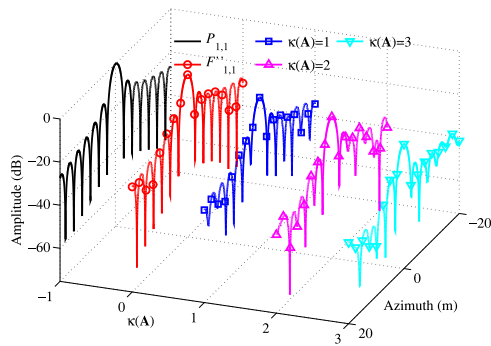


Fig. 14. Sectional plots of false scatterers  $F''_{1,1}$  versus condition number.

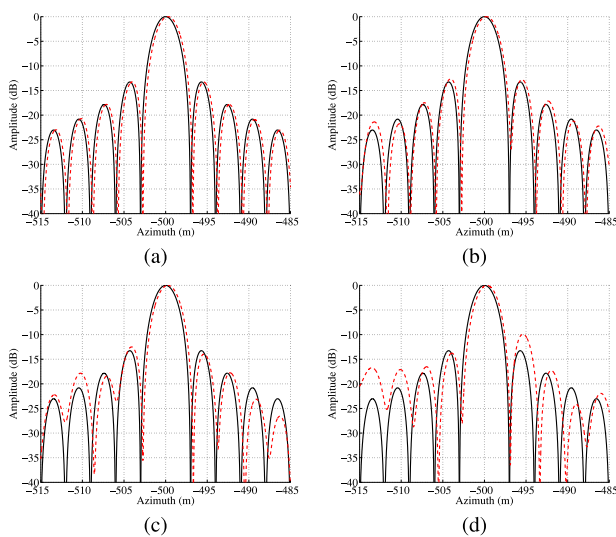


Fig. 15. Normalized sectional plots of the collaborative deception jamming results versus condition number. (a) Contrast false scatterer  $F''_{1,1}$ . (b)  $\kappa(\mathbf{A}) = 1$ . (c)  $\kappa(\mathbf{A}) = 2$ . (d)  $\kappa(\mathbf{A}) = 3$ .

TABLE IV  
COLLABORATIVE DECEPTION JAMMING QUALITY INDEXES WITH  
MEASUREMENT ERROR OF SCATTERER  $F_{1,1}$  VERSUS CONDITION NUMBER

|                          | IRW(m) | PSLR(dB) | ISLR(dB) | Range positional error(m) | Azimuth positional error(m) |
|--------------------------|--------|----------|----------|---------------------------|-----------------------------|
| $F''_{1,1}$              | 2.66   | -13.26   | -10.42   | 0.10                      | -0.30                       |
| $\kappa(\mathbf{A}) = 1$ | 2.64   | -12.63   | -9.78    | 0.10                      | -0.25                       |
| $\kappa(\mathbf{A}) = 2$ | 2.68   | -12.51   | -10.05   | 0.10                      | -0.25                       |
| $\kappa(\mathbf{A}) = 3$ | 2.61   | -9.93    | -7.54    | 0.10                      | -0.30                       |

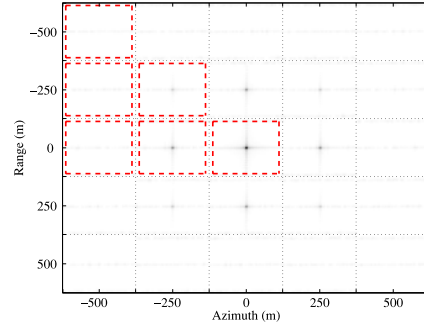


Fig. 16. Deception jamming result with measurement error.

be guaranteed. When  $\kappa(\mathbf{A}) = 3$ , the PSLR and ISLR of the false scatterer increase seriously, which in turn means that the neighboring scatterers will be affected by the leaking energy. Although the LLS estimator performed by collaborative receivers improves the accuracy of deception jamming, the optimal layout is still necessary for further performance improvement.

### C. Effect of Error Versus the Distance Between the False Scatterer and Jammer

To show the effect of error on deception jamming versus the distance between the false scatterer and jammer, two receivers  $D_1$  and  $D_2$ , whose locations follow the optimal layout given in Section III, are set for deception jamming modulation. The imaging results of the false scatterer array are shown in Fig. 16.

Notice that only the false scatterers near the center, at which the jammer locates, can be coherently imaged in Fig. 16. Nevertheless, the amplitudes of the false scatterers get weaker with their distance from the center increasing. The false scatterer in the center of the scene, say  $F'_{3,3}$ , achieves the similar quality as the real scatterer  $P_{3,3}$ . Moreover, it is seen that the scatterers near the center ( $F'_{2,3}$ ,  $F'_{3,2}$ ,  $F'_{3,4}$ , and  $F'_{4,3}$ ) get weaker in amplitude than  $F'_{3,3}$ , while the scatterers farther ( $F'_{2,2}$ ,  $F'_{2,4}$ ,  $F'_{4,2}$ , and  $F'_{4,4}$ ) become much weaker, which can barely be seen in the imaging result. The other scatterers that are much farther away from the center cannot be coherently focused in the image. The sectional plots of scatterers distributing in different distances from the center, which are surrounded by the dashed lines in Fig. 16, are given in Fig. 17.

In Fig. 17, the solid line denotes the sectional plot of the real scatterer as a reference. The other sectional plots are the false

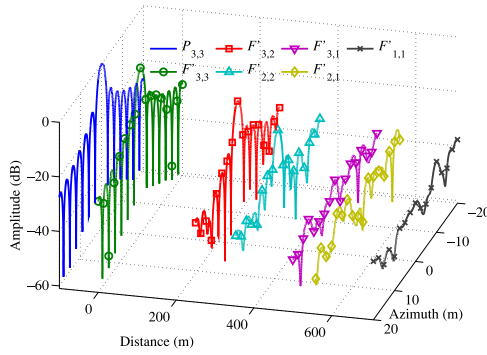
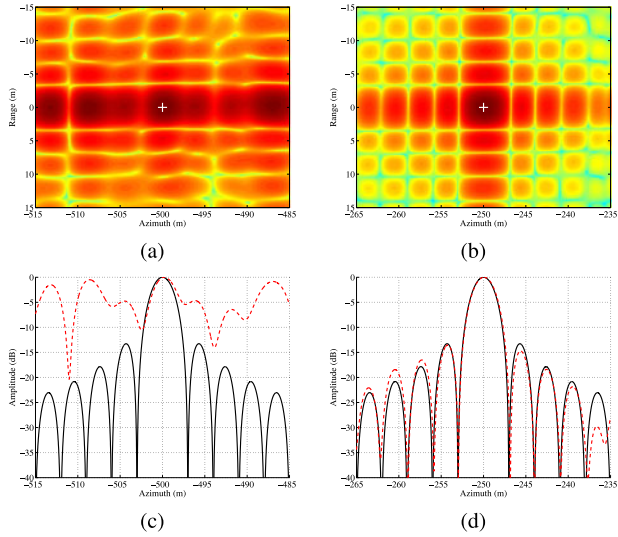


Fig. 17. Sectional plots of false scatterers versus distance.

Fig. 18. Deception jamming results and normalized sectional plots of false scatterers. (a) Image of  $F'_{3,1}$ . (b) Image of  $F'_{3,2}$ . (c) Sectional plot of  $F'_{3,1}$ . (d) Sectional plot of  $F'_{3,2}$ .

scatterers sorted according to their distances from the center and marked by different symbols. According to (43), the error level increases with the increasing of the distance between the false scatterers and jammer. The false scatterers, whose distances from the center are less than 400 m, can be vaguely focused. For the farther false scatterers, the coherence of the deception jamming reduces seriously, so their main lobes are buried in the side lobes. False scatterers  $F'_{3,1}$  and  $F'_{3,2}$  are chosen for further contrastive analysis.

The false scatterer  $F'_{3,1}$ , which locates far away from the center, defocuses seriously. As shown in Fig. 18(a), its main lobe can hardly be distinguished from the side lobes. The false scatterer  $F'_{3,2}$  is imaged better than  $F'_{3,1}$  as it is nearer to the center than the latter. It is observed in Fig. 18(b) that the main lobe in azimuth is well focused, whereas the side lobes are not ideally symmetrical. These results agree with the theoretical calculation in (43). That is, the effect of error on the deception jamming becomes dominant as the distance between the false scatterer and jammer increases. The normalized sectional plots are given in Fig. 18(c) and (d). In Fig. 18(c), the sectional plot

TABLE V  
DECEPTION JAMMING QUALITY INDEXES WITH MEASUREMENT ERROR  
VERSUS DISTANCE

|            | IRW(m) | PSLR(dB) | ISLR(dB) | Range positional error(m) | Azimuth positional error(m) |
|------------|--------|----------|----------|---------------------------|-----------------------------|
| $P_{3,1}$  | 2.66   | -13.26   | -10.42   | —                         | —                           |
| $F'_{3,1}$ | 2.83   | -0.50    | 5.58     | 0.10                      | -0.20                       |
| $P_{3,2}$  | 2.66   | -13.27   | -10.42   | —                         | —                           |
| $F'_{3,2}$ | 2.69   | -13.54   | -10.48   | 0.05                      | -0.05                       |

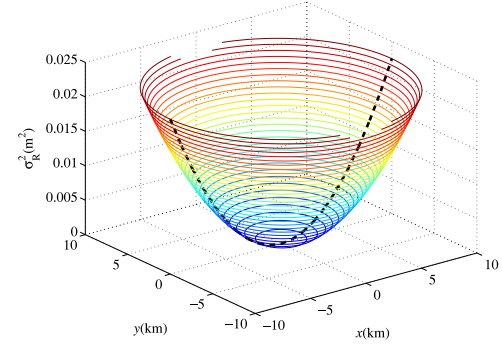


Fig. 19. Variances of the instantaneous slant range differences with different locations.

of  $F'_{3,1}$  (dashed line) distorts seriously from the Sinc function. The sectional plot of  $F'_{3,2}$  in Fig. 18(d) has the similar quality as the main lobe of the real one (solid line), while its side lobes are worse than that of the real one. The evaluation indexes are listed in Table V.

It is implied in Table V that the IRW of  $F'_{3,1}$  expands by 6.39% compared to the real scatterer  $P_{3,1}$ . But the PSLR and ISLR mean that the energy of the main lobe leaks to the side lobes seriously. Being located nearer to the center, the false scatterer  $F'_{3,2}$  is less affected by the error. Its IRW expands by 1.13%, PSLR and ISLR increase by 2.03% and 0.58%, respectively. Therefore, under the error circumstances, the effectiveness of synergy netting deception jamming can only be guaranteed in a small area around the jammer.

To verify (43), 5000 Monte-Carlo simulations have been carried out for the scatterers, which distribute in the square area around the jammer, ranging from -10 to 10 km. The contours of  $\sigma_R^2$  are given in Fig. 19.

The dashed line in Fig. 19 is determined by (43), which matches the simulation results. When the distance between the false scatterer and jammer increases, the performance of the deception jamming degrades rapidly. This thereby calls for collaborative receivers under the error circumstances to eliminate the effect of the measurement error on the deception jamming.

#### D. Collaborative Deception Jamming

In this simulation, the receivers are deployed according to the optimal layout addressed in Section IV-B. To evaluate the performance of collaborative deception jamming, 24 receivers are used. The false scatterers resulting from the collaborative

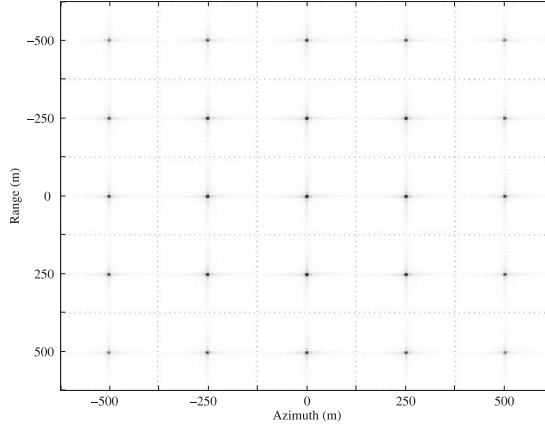


Fig. 20. Imaging results of collaborative deception jamming.

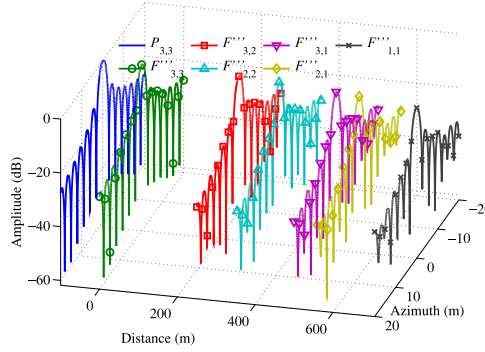


Fig. 21. Sectional plots of collaborative deception jamming false scatterers versus distance.

deception jamming are denoted by  $F'''_{k,l}$ . The imaging results of the false scatterer array are shown in Fig. 20.

Compared to the jamming result obtained utilizing two receivers, the collaborative deception jamming is able to generate focused deception jamming in a larger area. All the false scatterers are well imaged due to the error reduction effect of LLS estimation. Their sectional plots are also given in Fig. 21 according to their distances.

The Sinc function shapes of all these false scatterers are guaranteed with only small amplitudes loss versus their distance from the center. The amplitudes of these false scatterers are illuminated in Fig. 22. The amplitudes of the false scatterers obtained utilizing two receivers, which are given in Section V-C, are also plotted in the same figure for comparison.

In Fig. 22, the solid line denotes the amplitude curve obtained utilizing two receivers and the dashed line denotes that obtained using 24 collaborative receivers. The solid line reduces quickly to  $-35$  dB with the distance increasing. The deception jamming finally degenerates into incoherent noise. But the barrage jamming effect can not be achieved because the loss of coherent processing gain. Thus, the deception jamming is failed and buried in the side lobes of the real scatterers. When collaborative receivers are introduced, the amplitudes of the false scatterers reduce much slower with the distance increasing. The energy

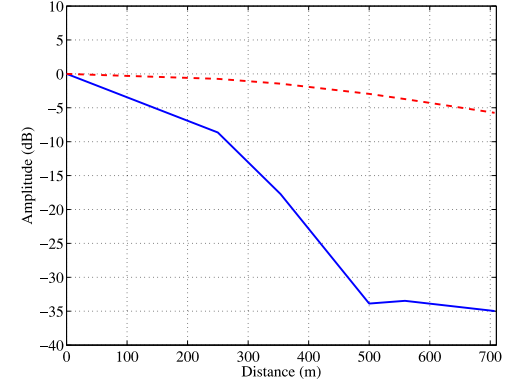
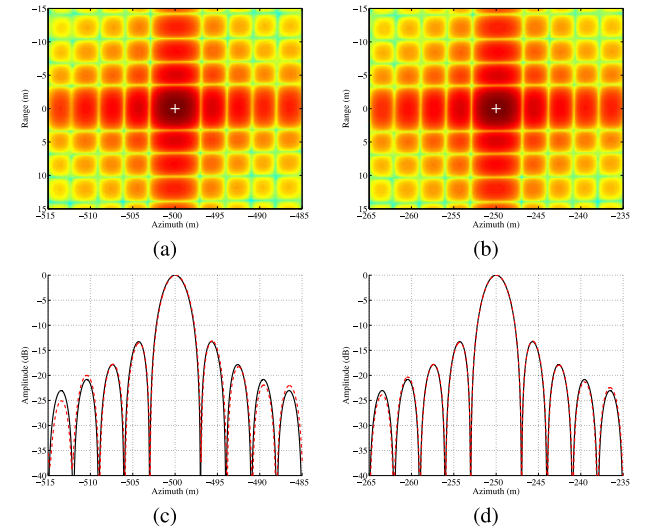


Fig. 22. Amplitude of false scatterers versus distance.

Fig. 23. Deception jamming results and normalized sectional plots of collaborative deception jamming false scatterers. (a) Image of  $F'''_{3,1}$ . (b) Image of  $F'''_{3,2}$ . (c) Sectional plot of  $F'''_{3,1}$ . (d) Sectional plot of  $F'''_{3,2}$ .

loss at the distance  $700$  m is about  $5$  dB. This is due to the error reduction effect of the LLS estimation utilizing collaborative receivers. Therefore, the introduction of collaborative receivers enlarges the deception jamming range effectively under error circumstances.

To further reveal the effectiveness of the collaborative deception jamming, the scatterers  $F'''_{3,1}$  and  $F'''_{3,2}$  are replotted in Fig. 23 for comparison. Meanwhile, their sectional plots are provided as well. It is observed from Fig. 23 that the collaborative deception jamming scatterers achieve the similar imaging quality as the real ones shown in Fig. 18(a) and (c), which can be further confirmed by the evaluation indexes listed in Table VI.

In order to study the performance of the collaborative deception jamming, 5000 Monte-Carlo simulations have been performed for different receiver numbers. When  $\kappa(\mathbf{A}) = 1$ , two receivers are added as a module each time. The curves of the normalized variance with different receiver numbers are plotted in Fig. 24. It is seen that the simulated curve (marked by “ $\times$ ”) is very close to the inverse curve (solid line). When  $\kappa(\mathbf{A}) = 2$

TABLE VI  
IMAGING QUALITY INDEXES OF THE DECEPTION JAMMING UTILIZING COLLABORATIVE RECEIVERS

| IRW(m)       | PSLR(dB) | ISLR(dB) | Range positional error(m) | Azimuth positional error(m) |
|--------------|----------|----------|---------------------------|-----------------------------|
| $F_{3,1}'''$ | 2.67     | -12.66   | -10.39                    | 0.10                        |
| $F_{3,2}'''$ | 2.66     | -12.94   | -10.38                    | 0.05                        |

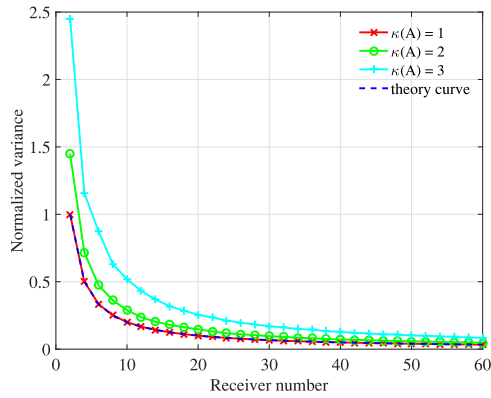


Fig. 24. Variation of the normalized variance with the receiver number.

and  $\kappa(\mathbf{A}) = 3$ , the receivers are deployed randomly, and the curves obtained are marked by “○” and “+,” respectively. In these cases, the variance also descends as the receiver number increases due to the error reduction effect of LLS estimator. However, the performance of error reduction is worse than that of the optimal layout with  $\kappa(\mathbf{A}) = 1$ .

Notice that the variance drops rapidly when the receiver number increases from 2 to 20, which confirms the effectiveness of the collaborative receivers in terms of error suppression. However, the decrease of normalized variance slows down as the receiver number further increases. On the other hand, when the collaborative receiver number becomes larger, the complexity of the jamming system increases but little benefits for error elimination can be gained. Therefore, it is suggest to adopt 20–30 receivers in the collaborative deception jamming system.

#### E. Scene Deception Jamming Simulation

For general application, we consider the deception jamming for large terrain scene. The simulation parameters are set the same as those listed in Table I.

In Fig. 25 (a), the real scene includes part of the coastal city and two freighters in the ocean. The false scene for deception jamming is designed according to the scattering characteristics of the SAR images. Two false wharves are set beyond the coastline to confuse the real terrain. In the simulation of deception jamming in Fig. 25(b), the details of the false wharves relative to the different types of terrain and different structures of buildings are included, which will disturb the understanding of SAR image. Another two false freighters are also modulated to the real SAR echo. They are designed appearing

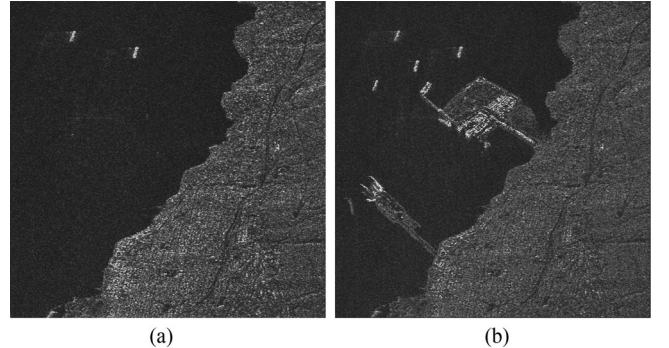


Fig. 25. Large terrain scene deception jamming simulation with pure background. (a) Real scene. (b) Deception jamming scene.

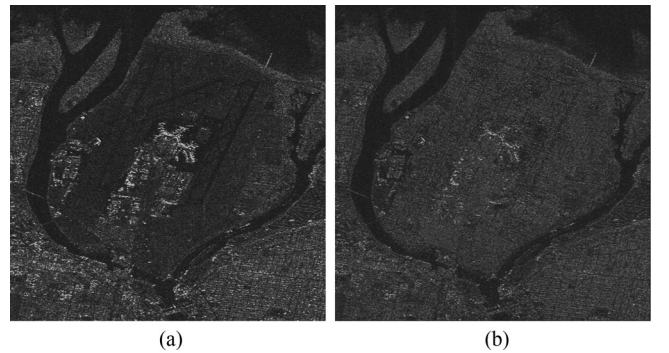


Fig. 26. Large terrain scene deception jamming simulation with complex background. (a) Real scene. (b) Deception jamming scene.

near the real freighters with the similar scattering characteristics as the real ones, which provide the protection for the real targets. The imaging indexes evaluated in the former simulations ensure the imaging quality of the false target. Therefore, the fidelity of the deception jamming can be guaranteed. It can be observed in Fig. 25 that the simulation results for the large-scene deception jamming verifies the effectiveness of the proposed algorithm for synergy netting deception jamming.

When the real terrain to be protected is not as pure as the ocean background in Fig. 25, the false terrain template has to be carefully designed with *a priori* information about the real terrain.

Fig. 26 (a) shows a real terrain scene with strong scattering building in the ground. The strong scatterers in the real scene can hardly be covered by the false city deception jamming. Therefore, the false scene is deployed around the building such that the shape of the real building is hidden in the false scene, which effectively protects the building from being recognized. How to design the false scene template to fit the real terrain is another interesting research topic, which is our future work.

## VI. CONCLUSION

In this paper, the optimal layout for receivers is proposed to improve the performance of the synergy netting deception jamming system under error circumstances. Besides, a collaborative deception jamming scheme is suggested to further reduce the

measurement error. In particular, the synergy netting deception jamming algorithm utilizes multiple receivers to provide high accurate measurements for TDOAs instead of reconnoitering the SAR kinematic parameters with low accuracy. This considerably improves the performance of SAR deception jamming algorithm without knowing the detailed SAR kinematic parameters. The simulation results indicate that the false scatterers generated by the proposed algorithm under error circumstances achieve the similar imaging evaluation indexes as the real scatterers, which verifies the effectiveness and fidelity of the proposed approach.

## APPENDIX

### PROOF OF THE OPTIMAL COLLABORATIVE RECEIVERS LAYOUT

*Theorem 1:* If the condition number of  $\mathbf{A}_n \in R^{2n \times 2}$  equals 1, then  $\kappa(\mathbf{A}_{n+1}) = 1$ , where

$$\mathbf{A}_{n+1} = \begin{pmatrix} \mathbf{A}_n \\ \mathbf{E}_{n+1} \end{pmatrix}$$

with  $\mathbf{E}_{n+1}$  being an orthogonal matrix such that  $\mathbf{E}_{n+1}\mathbf{E}_{n+1}^T = \mathbf{E}_{n+1}^T\mathbf{E}_{n+1} = \sigma_{n+1}^2 \mathbf{I}_2$ . Here,  $\sigma_{n+1}$  is the singular value of  $\mathbf{E}_{n+1}\mathbf{E}_{n+1}^T$ .

*Proof:* The recurrence method is utilized for the proof. When  $n = 1$ , the optimality of the isosceles right triangle layout has been proved in Section III. Therefore, the condition number of  $\mathbf{A}_n$  equals 1 for  $n = 1$ . The singular value decomposition (SVD) of  $\mathbf{A}_n$  is

$$\mathbf{A}_n = \mathbf{U}\Sigma\mathbf{V}^T \quad (\text{A.1})$$

where  $\mathbf{U} \in R^{2n \times 2n}$  and  $\mathbf{V} \in R^{2 \times 2}$  are the orthogonal matrixes,  $\Sigma$  is a  $2n \times 2$  diagonal matrix with nonnegative singular values on the diagonal. Consequently, the SVD of  $\mathbf{A}_n^T\mathbf{A}_n$  is

$$\mathbf{A}_n^T\mathbf{A}_n = \mathbf{V}\Sigma^T\Sigma\mathbf{V}^T. \quad (\text{A.2})$$

The minimum and maximum singular values of  $\mathbf{A}_n^T\mathbf{A}_n$  equal the squared values of the maximum and minimum singular values of  $\mathbf{A}_n$ , which are denoted by  $\sigma_{\max}$  and  $\sigma_{\min}$ , respectively. So we have

$$\kappa(\mathbf{A}_n^T\mathbf{A}_n) = \frac{\sigma_{\max}^2}{\sigma_{\min}^2} = [\kappa(\mathbf{A}_n)]^2 = 1. \quad (\text{A.3})$$

From (A3), we get that  $\sigma_{\max} = \sigma_{\min} = \sigma_n$ . Similarly, the relationship between  $\kappa(\mathbf{A}_n^T\mathbf{A}_n)$  and  $\kappa(\mathbf{A}_n)$  can also be extended to  $\mathbf{A}_{n+1}$ . According to the relationship between  $\mathbf{A}_{n+1}$  and  $\mathbf{A}_n$ , we get that

$$\begin{aligned} \mathbf{A}_{n+1}^T\mathbf{A}_{n+1} &= (\mathbf{A}_n^T \quad \mathbf{E}_{n+1}^T) \begin{pmatrix} \mathbf{A}_n \\ \mathbf{E}_{n+1} \end{pmatrix} \\ &= \mathbf{A}_n^T\mathbf{A}_n + \mathbf{E}_{n+1}^T\mathbf{E}_{n+1} \\ &= \mathbf{V}\Sigma^T\Sigma\mathbf{V}^T + \sigma_{n+1}^2 \mathbf{I}_2 \\ &= \sigma_n^2 \mathbf{V}\mathbf{V}^T + \sigma_{n+1}^2 \mathbf{V}\mathbf{V}^T \\ &= (\sigma_n^2 + \sigma_{n+1}^2) \mathbf{I}. \end{aligned} \quad (\text{A.4})$$

The condition number of  $\mathbf{A}_{n+1}^T\mathbf{A}_{n+1}$  can also be calculated utilizing its singular values, that is,

$$\kappa(\mathbf{A}_{n+1}^T\mathbf{A}_{n+1}) = \frac{\sigma_n^2 + \sigma_{n+1}^2}{\sigma_n^2 + \sigma_{n+1}^2} = 1. \quad (\text{A.5})$$

Thus, we have

$$\kappa(\mathbf{A}_{n+1}) = \sqrt{\kappa(\mathbf{A}_{n+1}^T\mathbf{A}_{n+1})} = 1. \quad (\text{A.6})$$

■

It follows from Theorem 1 that two receivers, which construct a isosceles right triangle with the jammer, are organized as a basic module for collaborative deception jamming system extension. When  $n = 1$ , the optimality of the isosceles right triangle layout has been proved. With the increasing of  $n$ , the addition of a two-receiver module keeps the optimal condition number of the jamming system before extension, which can be verified by utilizing Theorem 1. It should be pointed out that neither of the receivers are collinear with the jammer.

Denote the two receivers of the  $(n+1)$ th module by  $D_{n+1}$  and  $D'_{n+1}$ , respectively.  $r_{n+1}$  is the distance from  $D_{n+1}$  to the jammer, which equals that between  $D'_{n+1}$  and the jammer. The  $\phi_{n+1}$  is the angle between  $D_{n+1}$  and positive direction of axis  $x$ , and  $\phi'_{n+1} = \phi_{n+1} + 90^\circ$ . Then, the  $(n+1)$ th module can be denoted as

$$\mathbf{E}_{n+1} = r_{n+1} \begin{pmatrix} \cos \phi_{n+1} & \sin \phi_{n+1} \\ -\sin \phi_{n+1} & \cos \phi_{n+1} \end{pmatrix}. \quad (\text{A.7})$$

Concatenating  $\mathbf{A}_n$  and  $\mathbf{E}_{n+1}$  in column dimension, we can get an optimal coefficient matrix to calculate the deception jamming parameters with  $2(n+1)$  collaborative receivers.

## REFERENCES

- [1] G. Satalino, A. Balenzano, F. Mattia, and M. W. J. Davidson, "C-band SAR data for mapping crops dominated by surface or volume scattering," *IEEE Geosci. Remote Sens. Lett.*, vol. 11, no. 2, pp. 384–388, Feb. 2014.
- [2] C. Wang, H. Zhang, F. Wu, S. Jiang, B. Zhang, and Y. Tang, "A novel hierarchical ship classifier for COSMO-SkyMed SAR data," *IEEE Geosci. Remote Sens. Lett.*, vol. 11, no. 2, pp. 484–488, Feb. 2014.
- [3] B. Hou, W. Yang, S. Wang, and X. Hou, "SAR image ship detection based on visual attention model," in *Proc. IEEE Int. Geosci. Remote Sens. Symp.*, 2013, pp. 2003–2006.
- [4] A. S. Komarov, V. Zabeline, and D. G. Barber, "Ocean surface wind speed retrieval from c-band SAR images without wind direction input," *IEEE Trans. Geosci. Remote Sens.*, vol. 52, no. 2, pp. 980–990, Feb. 2014.
- [5] F. Lombardini and F. Cai, "Temporal decorrelation-robust SAR tomography," *IEEE Trans. Geosci. Remote Sens.*, vol. 52, no. 9, pp. 5412–5421, Sep. 2014.
- [6] J. Chen, M. Iqbal, W. Yang, P. B. Wang, and B. Sun, "Mitigation of azimuth ambiguities in spaceborne stripmap SAR images using selective restoration," *IEEE Trans. Geosci. Remote Sens.*, vol. 52, no. 7, pp. 4038–4045, Jul. 2014.
- [7] T. Nagler and H. Rott, "Retrieval of wet snow by means of multitemporal SAR data," *IEEE Trans. Geosci. Remote Sens.*, vol. 38, no. 2, pp. 754–765, Mar. 2000.
- [8] J. M. Lopez Sanchez and J. Fortunyguasch, "3-D radar imaging using range migration techniques," *IEEE Trans. Antennas Propag.*, vol. 48, no. 5, pp. 728–737, May 2000.
- [9] L. Rosenberg and D. A. Gray, "Constrained fast-time STAP techniques for interference suppression in multichannel SAR," *IEEE Trans. Aerosp. Electron. Syst.*, vol. 49, no. 3, pp. 1792–1805, Jul. 2013.

- [10] M. Tao, F. Zhou, J. Liu, Y. Liu, Z. Zhang, and Z. Bao, "Narrow-band interference mitigation for SAR using independent subspace analysis," *IEEE Trans. Geosci. Remote Sens.*, vol. 52, no. 9, pp. 5289–5301, Sep. 2014.
- [11] X. Song, P. Willett, S. Zhou, and P. B. Luh, "The MIMO radar and jammer games," *IEEE Trans. Signal Process.*, vol. 60, no. 2, pp. 687–699, Feb. 2012.
- [12] M. Soumekh, "SAR-ECCM using phase-perturbed LFM chirp signals and DRFM repeat jammer penalization," *IEEE Trans. Aerosp. Electron. Syst.*, vol. 42, no. 1, pp. 191–205, Jan. 2006.
- [13] H. X. Huang, Y. Y. Zhou, J. Wu, and Z. T. Huang, "A frequency-based inter/intra partly coherent jamming style to SAR," in *Proc. 2nd Int. Conf. Signal Process. Syst.*, 2010, pp. V2-434–V2-437.
- [14] W. Ye, R. Hang, S. X. Zhang, and L. Yan, "Study of noise jamming based on convolution modulation to SAR," in *Proc. Int. Conf. Comput. Mechatronics, Control Electron. Eng.*, 2010, pp. 169–172.
- [15] H. X. Huang, Y. Y. Zhou, W. L. Jiang, and Z. T. Huang, "A new time-delay echo jamming style to SAR," in *Proc. 2nd Int. Conf. Signal Process. Syst.*, 2010, pp. V3-14–V3-17.
- [16] D. Huang, "A novel forward-backward smoothing-based learning subspace method for recognition of radar targets," *Int. J. Pattern Recognit. Artif. Intell.*, vol. 13, no. 1, pp. 65–83, 2011.
- [17] D. Huang, "Application of generalized radial basis function networks to recognition of radar targets," *Int. J. Pattern Recognit. Artif. Intell.*, vol. 13, no. 6, pp. 945–962, 2011.
- [18] D. H. Dai, X. F. Wu, X. S. Wang, and S. P. Xiao, "SAR active-decoys jamming based on DRFM," in *Proc. IET Int. Conf. Radar Syst.*, 2007, pp. 1–4.
- [19] X. Lin, P. Liu, and G. Xue, "Fast generation of SAR deceptive jamming signal based on inverse range Doppler algorithm," in *Proc. IET Int. Radar Conf.*, 2013, pp. 1–4.
- [20] B. Zhao, J. Yang, G. Sun, F. Zhou, and Z. Bao, "A method of SAR fast repeater deception jamming for large false scene," *Dianzi Yu Xinxi Xuebao/J. Electron. Inf. Technol.*, vol. 34, no. 4, pp. 963–968, 2012.
- [21] F. Zhou, B. Zhao, M. Tao, X. Bai, B. Chen, and G. Sun, "A large scene deceptive jamming method for space-borne SAR," *IEEE Trans. Geosci. Remote Sens.*, vol. 51, no. 8, pp. 4486–4495, Aug. 2013.
- [22] Y. Zhu, G. Zhao, and Y. Zhang, "Research on SAR jamming technique based on man-made map," in *Proc. Int. Conf. Radar*, 2006, pp. 1–4.
- [23] B. Zhao, F. Zhou, and Z. Bao, "Deception jamming for squint SAR based on multiple receivers," *IEEE J. Sel. Topics Appl. Earth Observ. Remote Sens.*, vol. 8, no. 8, pp. 3988–3998, Aug. 2015.
- [24] F. Wen and Q. Wan, "Maximum likelihood and signal-selective TDOA estimation for noncircular signals," *J. Commun. Netw.*, vol. 15, no. 3, pp. 245–251, 2013.
- [25] Y. Liu and W. Zhu, "High precision TDOA measurement technique," *Aerosp. Electron. Warfare*, vol. 25, no. 2, pp. 48–50, 2009.
- [26] R. G. Wiley, *ELINT: The Interception and Analysis of Radar Signals*. Norwood, MA, USA: Artech House, 2006.
- [27] J. Y. Liu, J. Cai, X. Zhu, and W. Q. Wang, "On the inverse matrix of near-space elevation multi-aperture SAR imaging," in *Proc. Int. Conf. Comput. Problem-Solving*, 2011, pp. 186–189.
- [28] L. Kou, X. Wang, M. Xiang, and M. Zhu, "Interferometric estimation of three-dimensional surface deformation using geosynchronous circular SAR," *IEEE Trans. Aerosp. Electron. Syst.*, vol. 48, no. 2, pp. 1619–1635, Apr. 2012.
- [29] Y. P. Wang, "Locating calibrators in airborne InSAR calibration," in *Proc. IEEE Int. Geosci. Remote Sens. Symp.*, 2003, vol. 7, pp. 4515–4517.
- [30] B. C. Barber, "Theory of digital imaging from orbital synthetic aperture radar," *Int. J. Remote Sens.*, vol. 6, no. 7, pp. 1009–1057, 1985.
- [31] J. Chen, D. Zeng, and T. Long, "High precision radar echo modelling and simulation method," in *Proc. Int. Conf. Radar*, 2008, pp. 469–473.
- [32] G. Sun *et al.*, "A new signal model for a wideband synthetic aperture imaging sensor," *Can. J. Remote Sens.*, vol. 37, no. 2, pp. 171–183, 2011.



**Bo Zhao** (M'15) was born in Henan, China, in 1986. He received the B.Sc. and Ph.D. degrees from Xidian University, Xi'an, China, in 2010 and 2015, respectively.

He is currently a Postdoctoral Researcher with the Institute of Multi-Dimensional Signal Processing, Shenzhen University, Shenzhen, China. His research interests include radar imaging, synthetic aperture radar countermeasure, and compressive sensing.



**Lei Huang** (M'07–SM'14) was born in Guangdong, China. He received the B.Sc., M.Sc., and Ph.D. degrees in electronic engineering from Xidian University, Xi'an, China, in 2000, 2003, and 2005, respectively.

From 2005 to 2006, he was a Research Associate with the Department of Electrical and Computer Engineering, Duke University, Durham, NC, USA. From 2009 to 2010, he was a Research Fellow with the Department of Electronic Engineering, City University of Hong Kong and a Research Associate with the Department of Electronic Engineering, The Chinese University of Hong Kong. From 2011 to 2014, he was a Professor with the Department of Electronic and Information Engineering, Harbin Institute of Technology Shenzhen Graduate School. Since November 2014, he has been with the Department of Information Engineering, Shenzhen University, Shenzhen, China, where he is currently a Distinguished Professor. His research interests include spectral estimation, array signal processing, statistical signal processing, and their applications in radar, navigation, and wireless communications.

Dr. Huang is an Associate Editor for the *IEEE TRANSACTIONS ON SIGNAL PROCESSING AND Digital Signal Processing*.



**Feng Zhou** (M'11) was born in Henan, China, in 1980. He received the M.Sc. and Ph.D. degrees in signal and information processing from Xidian University, Xi'an, China, in 2004 and 2007, respectively.

He is currently a Professor with the National Laboratory of Radar Signal Processing, Xidian University. His research interests include radar imaging and jamming suppression.

Prof. Zhou was granted the program for New Century Excellent Talents in University in China and received the Young Scientist Award from XXXI URSI General Assembly and Scientific Symposium Committee.



**Jihong Zhang** was born in Jiangsu, China, in 1964. He received the B.Eng., M.Eng., and Ph.D. degrees from Southeast University, Nanjing, China, in 1986, 1989, and 1992, respectively.

From November 1995 to February 1996, he was a Visiting Scholar at the University of Central Lancashire, U.K. From April 1997 to November 1997, he was a Visiting Scholar at Soka University, Japan. From May 2000 to June 2000, he was a Visiting Scholar at the University of Liverpool, U.K. He is a Professor with the College of Information Engineering, Shenzhen University, Shenzhen, China. His research interests include digital signal processing, artificial neural network, fuzzy logic, ant colony optimization, and their applications in wireless communications and video/image/speech processing.